lajss.org
Latin American Journal of Solids and Structures
www.lajss.org

Nonlinear dynamic response of functionally graded half-cylinder sandwich shells with elastic boundary conditions subjected to explosive loading

Ngoc Anh Vu[a], Truong Son Le[b], Trung Thanh Tran[c], TD Pham[d], Quoc-Hoa Pham[e], Nhan Thinh Hoang[f*]

[a]Institute of Techniques for Special Engineering, Le Quy Don Technical University, Hanoi, Vietnam. Email: ngocanh.vu@lqdtu.edu.vn
[b]Faculty of Mechanical Engineering, Le Quy Don Technical University, Hanoi, Vietnam. Email: letruongson01@gmail.com
[c]Faculty of Mechanical Engineering, Le Quy Don Technical University, Hanoi, Vietnam. Email: tranthanh0212@gmail.com
[d]Faculty of Aerospace Engineering, Le Quy Don Technical University, Hanoi, Vietnam. Email: pham.thanh-dong@lqdtu.edu.vn
[e]Faculty of Mechanical Engineering, Tran Dai Nghia University, Ho Chi Minh City, Vietnam. Email: quochoavhp@gmail.com
[f]Institute of International Education, Nguyen Tat Thanh University, Ho Chi Minh City, Vietnam. Email: htnhan@ntt.edu.vn

* Corresponding author

Abstract

This study investigates the nonlinear dynamic of functionally graded half-cylinder sandwich (FGhCS) shells with elastic boundary conditions (EBCs) subjected to explosive loading (EL). The main goal is to establish an efficient finite element framework that can accurately capture the coupled mechanical responses arising from geometric and material nonlinearities. The sandwich shell consists of a ceramic core sandwiched between two functionally graded material (FGM) face sheets, whose effective properties vary continuously through the thickness according to a power-law distribution. Nonlinear geometric effects, including mid-plane stretching and large-amplitude deformation, are incorporated through the von Kármán-type nonlinear strain–displacement relations. The governing equations of motion are systematically derived from Hamilton's principle within a novel first-order shear deformation theory (n-FSDT), which enhances both accuracy and computational efficiency compared with conventional FSDT formulations. The proposed finite element formulation is thoroughly validated against available benchmark results, demonstrating excellent agreement and significant reduction in computational cost. A detailed parametric study is then conducted to examine the influence of geometric parameters, power-law index, and boundary stiffness on the nonlinear dynamic response of FGhCS shells. The results reveal that material gradation and elastic boundary stiffness play critical roles in mitigating the adverse effects of explosive loads, offering practical insights for the optimal design and manufacturing of FGhCS shells under extreme dynamic environments.

Keywords

Haft-hyperboloid shells; Elastic boundary conditions; MITC4; FGM; FEM.

Graphical Abstract

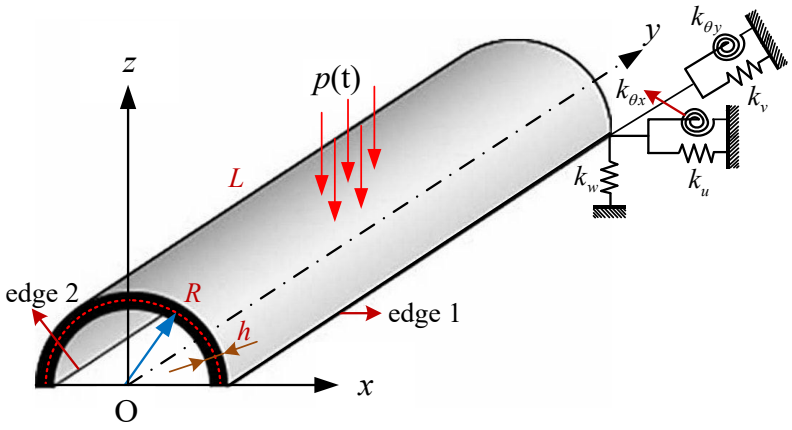

Geometric models of the FGhCS shell with EBCs at edges 1 and 2

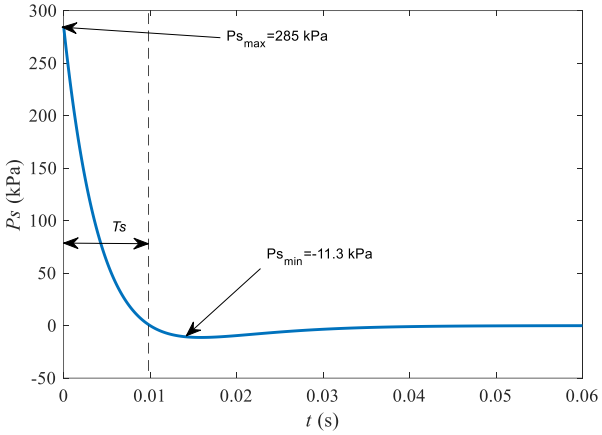

Explosive pressure function

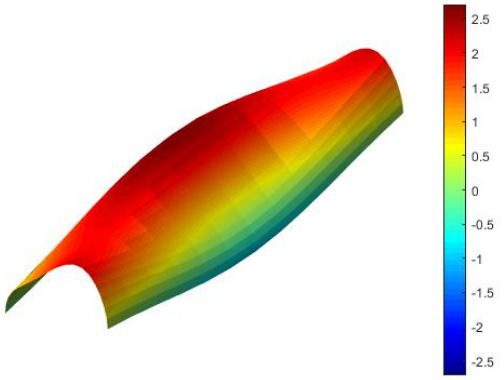

6th mode

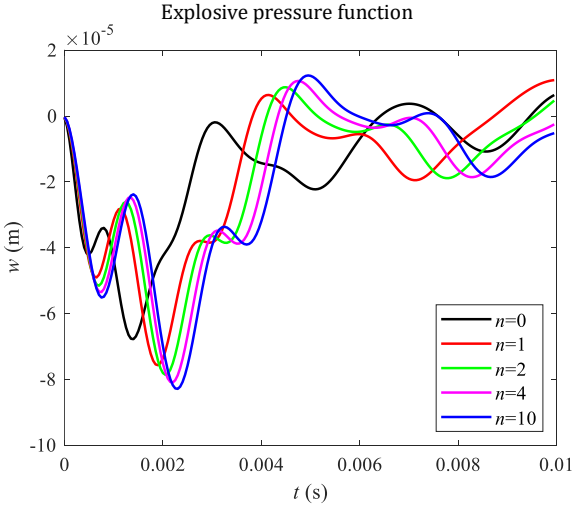

The nonlinear centre deflection response

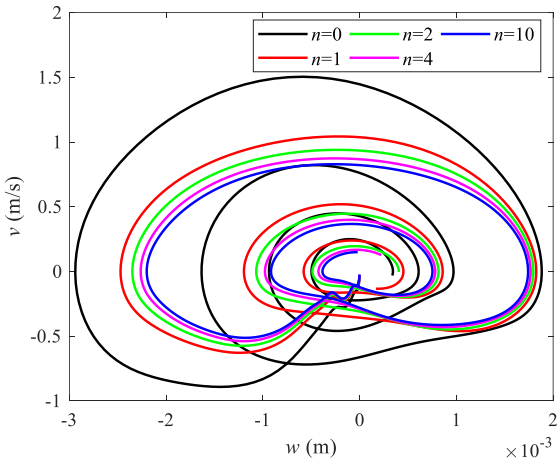

Phase orbit (2D-view)

1 INTRODUCTION

A sandwich structure generally comprises two thin, high-stiffness face sheets bonded to a comparatively thick and low-density core. This configuration provides excellent bending stiffness, low mass density, and superior acoustic and thermal insulation properties, making them highly attractive in aerospace, marine, and automotive applications. However, their structural integrity can be compromised by stress concentrations in load-bearing regions and interfacial delamination between layers caused by geometric or material discontinuities. As a result, a thorough understanding and precise modeling of the mechanical behavior of sandwich plates and shells are required for the safe and efficient design of advanced lightweight structures.

During the last few decades, significant advancements have been made in the formulation of higher-order and refined deformation theories, with the primary objective of providing more precise and computationally efficient modeling frameworks for the analysis of sandwich structures. These include the first-order shear deformation theory (FSDT) (Do & Tran, 2024, 2026; Hosseini-Hashemi et al., 2010; Trai et al., 2025; Tran, 2026), higher-order shear deformation theory (HSDT) (Do et al., 2025; Le & Tran, 2024; Nguyen, Nguyen, et al., 2024; Nguyen et al., 2022; Reddy, 2000; Talha & Singh, 2010; Zenkour, 2013b), nth-order shear deformation theory (Yaghoobi & Fereidoon, 2014), and quasi-3D theories (Le et al., 2026; Mantari & Soares, 2013), as well as several refined and hybrid models that account for transverse shear and normal deformation effects with improved accuracy. Numerous studies have employed these formulations to investigate the static, dynamic, and stability responses of FGM sandwich structures. For instance, Zenkour (2013a) presented a closed-form analytical solution for the static bending behavior of FGM sandwich plates, whereas, while Zarga (2019) proposed an exact quasi-3D formulation for thermo-mechanical bending analysis. Alibeigloo and Alizadeh (2015) analyzed static and free vibration responses of FGM sandwich plates using the state-space differential quadrature method (DQM) in conjunction with the third-order shear deformation theory (TSDT). Natarajan and Manickam (2012) conducted a comprehensive investigation on the bending and vibration characteristics of FGM sandwich plates using accurate higher-order plate models. Neves et al. (2017) further investigated buckling and static responses based on zig-zag and warping-enhanced higher-order theories, emphasizing the role of interlaminar continuity. Liu and Jeffers (2017) integrated a layerwise displacement theory with isogeometric analysis (IGA) to enhance geometric representation and interfacial accuracy in laminated and sandwich plates. Later studies extended these concepts to shell configurations, such as the thermal buckling of FGM sandwich truncated conical shells by Duc et al. (2018) and the free vibration of FGM doubly-curved shallow shells by Chen et al. (2017).

The vibration and dynamic behavior of shell structures have long been a central topic in structural mechanics. Foundational work by Leissa (1973) established theoretical frameworks for the dynamics of laminated composite shells, while numerous numerical approaches–including finite difference and Ritz methods (Chung, 1981), differential quadrature techniques (Loy et al., 1997; Shu & Du, 1997), and unified shell formulations (Jin et al., 2013)–have advanced their computational modeling. With the advent of functionally graded materials (FGMs), subsequent research focused on their influence on shell vibration and stability. Loy et al. (1999) and Pradhan et al. (2000) examined the vibration characteristics of FGM cylindrical shells under various boundary conditions, while Malekzadeh and Heydarpour (2012) accounted for thermal environments. More recent contributions have considered elastic foundations (Kim, 2015), porous distributions (Nguyen et al., 2023; Nguyen, Le, et al., 2024; Pham et al., 2023; Wang & Wu, 2017), and rotating conditions (Dang et al., 2022; Qin et al., 2019). The inclusion of stiffeners was also addressed by Tran et al. (2020); (Tu & Loi, 2016), highlighting the effect of structural reinforcement on vibrational behavior.

In parallel, several studies explored nonlinear dynamic responses and failure mechanisms of shell structures under extreme environments. Gupta et al. (2008) and Li et al. (2021) examined buckling and dynamic failure of spherical shells, Yin et al. (2023) investigated blast responses of cylindrical shells, and Liu et al. (2018) analyzed collision-induced buckling of subsea shells. Karakoti et al. (2022) further reported nonlinear transient responses of porous FG sandwich panels under blast and thermal loading. These studies collectively underscore the evolution from classical laminated shells to modern FGM and sandwich shells, emphasizing the necessity for robust, efficient finite element formulations capable of handling nonlinear, multiphysics, and transient phenomena.

Despite these advances, research on FGhCS shells remains limited–particularly concerning nonlinear dynamic responses subjected to EL and EBCs. Most existing studies focus on single-layer or fully graded shells, often neglecting the combined effects of material gradation, elastic supports, and extreme dynamic loads. Moreover, the coupling between geometric nonlinearity, material heterogeneity, and boundary flexibility remains an open challenge in predicting the true dynamic performance of such structures.

To address these gaps, the paper proposes an efficient finite element framework for analyzing the nonlinear

dynamic behavior of FGhCS shells supported by EBCs subjected to EL. The formulation is developed based on a n-FSDT incorporating von Kármán-type geometric nonlinearity, and the governing equations are systematically derived from Hamilton's principle. The proposed method is validated against existing benchmark solutions and subsequently employed in an extensive parametric study to evaluate the effects of geometric dimensions, gradation index, core thickness, and boundary stiffness on the nonlinear dynamic responses.

Beyond its theoretical contributions, this work has significant practical implications in defense, aerospace, and nuclear engineering. The results provide fundamental insights for the design of blast-resistant sandwich shells used in protective casings, missile fuselages, armored vehicles, and containment structures in nuclear facilities. Understanding how FGhCS shells respond under explosive and transient loads enables the development of lightweight yet resilient structural systems capable of withstanding impact, shock, and thermal-radiative coupling in extreme operational environments. Therefore, the findings of this study not only advance computational mechanics but also contribute to the design optimization of next-generation defense and energy systems that demand high strength-to-weight ratios and superior dynamic resistance.

2 MATHEMATICAL FORMULATION

2.1 The FGhCS shell model

The physical domain under consideration is a FGhCS shell subjected to EBCs applied along its longitudinal edges, as schematically illustrated in Figure 1. The shell has a length L, mean radius R, and total thickness h. The wall thickness comprises three perfectly bonded layers: a bottom FGM face sheet of thickness h_1, a homogeneous ceramic core of thickness h_2, and a top FGM face sheet of thickness h_3, satisfying $h = h_1 + h_2 + h_3$. The relative layer proportions are expressed by the thickness ratio $h_1 : h_2 : h_3$.

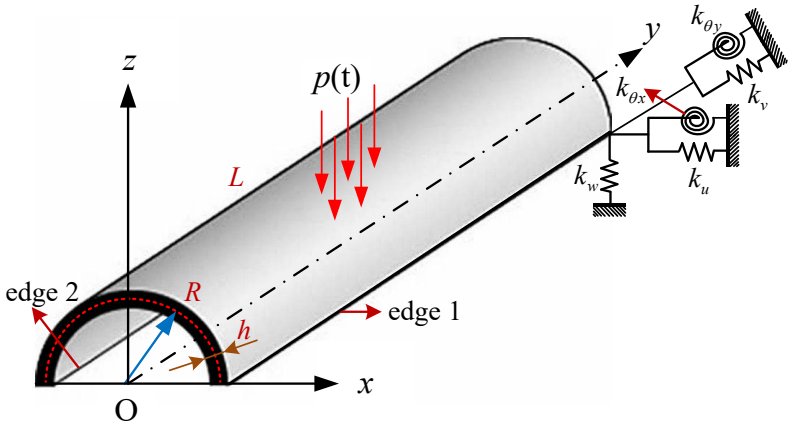

Figure 1 Geometric models of the FGhCS shell with EBCs at edges 1 and 2.

In the FGM face sheets, material properties vary smoothly through the thickness direction according to a power-law distribution of the ceramic and metallic constituents, whereas the ceramic core maintains uniform mechanical properties. The effective elastic modulus, mass density, and other mechanical parameters of the FGM layers are estimated using the rule of mixtures, ensuring a continuous transition of material properties across the interfaces.

The volume fraction $V_c^{(i)}$ of the ceramic in each layer is determined by

$$\begin{cases} V_c^{(1)} = \left(\dfrac{z - z_1}{z_2 - z_1}\right)^n & z \in [z_1; z_2] \\ V_c^{(2)} = 1 & z \in (z_2; z_3) \\ V_c^{(3)} = \left(\dfrac{z - z_4}{z_3 - z_4}\right)^n & z \in [z_3; z_4] \end{cases} \tag{1}$$

The effective material properties of FGhCS shell are defined by

$$P^{(i)}(z) = P_c V_c^{(i)} + P_m\left(1 - V_c^{(i)}\right), \quad i = 1,2,3 \tag{2}$$

where $P^{(i)}(z)$ represents the material characteristics of each layer, including the elastic modulus, Poisson's ratio, and mass density; n is the power-law index.

The EBCs are modeled through a combination of translational and rotational springs uniformly distributed along the longitudinal circumferential edges of the half-cylinder. This formulation enables realistic representation of partially restrained or flexible supports, ranging from simply supported to clamped-like conditions, depending on the stiffness of the springs. Such an approach captures the mechanical flexibility encountered in practical assemblies, such as curved panels, fuselage sections, or protective shell components under explosive loading.

2.2 Blast load model

The external load applied to the FGhCS shell is an explosive overpressure pulse. The time-dependent pressure function is proposed by Lam et al. (2004):

$$p(t) = 1.8Ps_{\max}(1 - t/T_s)e^{-\alpha t/T_s} \tag{3}$$

In this equation, $Ps_{\max}$ denotes the peak static overpressure (MPa), $\alpha = 1.7$ is a decay coefficient controlling the rate at which the pressure amplitude attenuates, and T_s is the positive phase duration of the blast pulse. The pressure rises instantaneously to its peak value $1.8Ps_{\max}$ at $t = 0$ and then decays exponentially with time, reaching zero at approximately $t = T_s$, as presented in Figure 2. This expression effectively captures the essential characteristics of a Friedlander-type blast wave, widely used to represent free-field or reflected explosions acting on structural surfaces.

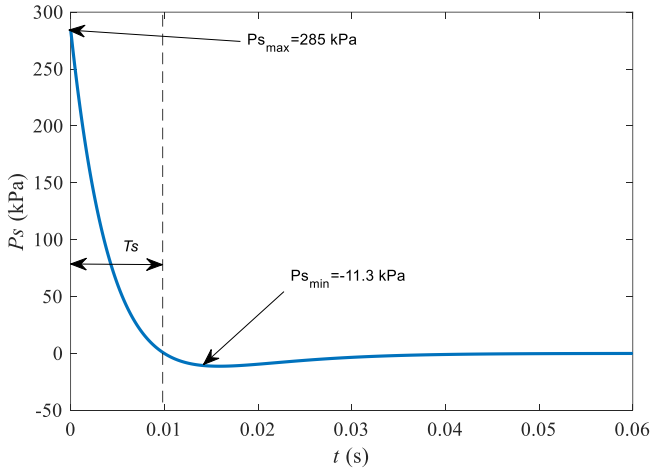

Figure 2 Explosive pressure function.

2.3 The displacement field

The displacement field according to the FSDT is defined by Reddy (2003):

$$\begin{cases} u\,(x,y,z,t) = u_0(x,y,t) + z\theta_x(x,y,t) \\ v\,(x,y,z,t) = v_0(x,y,t) + z\theta_y(x,y,t) \\ w\,(x,y,z,t) = w_0(x,y,t) \end{cases} \tag{4}$$

where u_0, v_0, w_0, θ_x and θ_y represent the displacement field variables. Specifically, u_0, v_0, and w_0 denote the mid-surface displacements in the x-, y- and z-directions, respectively, while θ_x and θ_y correspond to the rotations of the normal about the y- and x-axes. The adopted FSDT is well-suited for thin to moderately thick shells, providing a reliable balance between accuracy and computational efficiency.

The normal strain based on the von Kármán assumption is expressed by Reddy (2015):

$$\boldsymbol{\varepsilon} = \begin{Bmatrix} \varepsilon_{xx} \\ \varepsilon_{yy} \\ \gamma_{xy} \end{Bmatrix} = \begin{Bmatrix} \dfrac{\partial u}{\partial x} + 0.5\left(\dfrac{\partial w}{\partial x}\right)^2 \\ \dfrac{\partial v}{\partial y} + 0.5\left(\dfrac{\partial w}{\partial y}\right)^2 \\ \dfrac{\partial u}{\partial y} + \dfrac{\partial v}{\partial x} + \dfrac{\partial w}{\partial x}\dfrac{\partial w}{\partial y} \end{Bmatrix} = \begin{Bmatrix} \dfrac{\partial u_0}{\partial x} + 0.5\left(\dfrac{\partial w_0}{\partial x}\right)^2 \\ \dfrac{\partial v_0}{\partial y} + 0.5\left(\dfrac{\partial w_0}{\partial y}\right)^2 \\ \dfrac{\partial u_0}{\partial y} + \dfrac{\partial v_0}{\partial x} + \dfrac{\partial w_0}{\partial x}\dfrac{\partial w_0}{\partial y} \end{Bmatrix} + z\begin{Bmatrix} \dfrac{\partial \theta_x}{\partial x} \\ \dfrac{\partial \theta_y}{\partial y} \\ \dfrac{\partial \theta_x}{\partial y} + \dfrac{\partial \theta_y}{\partial x} \end{Bmatrix} \tag{5}$$

In matrix form:

$$\boldsymbol{\varepsilon} = \boldsymbol{\varepsilon}_m + z\boldsymbol{\kappa} \tag{6}$$

in which

$$\boldsymbol{\varepsilon}_m = \boldsymbol{\varepsilon}_m^L + \boldsymbol{\varepsilon}_m^{NL} = \begin{Bmatrix} \dfrac{\partial u_0}{\partial x} \\ \dfrac{\partial v_0}{\partial y} \\ \dfrac{\partial u_0}{\partial y} + \dfrac{\partial v_0}{\partial x} \end{Bmatrix} + 0.5 \begin{Bmatrix} \left(\dfrac{\partial w_0}{\partial x}\right)^2 \\ \left(\dfrac{\partial w_0}{\partial y}\right)^2 \\ 2\dfrac{\partial w_0}{\partial x}\dfrac{\partial w_0}{\partial y} \end{Bmatrix} \tag{7}$$

with $\boldsymbol{\varepsilon}_m^L$ is the linear membrane strain and $\boldsymbol{\varepsilon}_m^{NL}$ is the nonlinear membrane strain.

The nonlinear membrane strain $\boldsymbol{\varepsilon}_m^{NL}$ is rewritten by

$$\boldsymbol{\varepsilon}_m^{NL} = 0.5 \begin{Bmatrix} \left(\dfrac{\partial w_0}{\partial x}\right)^2 \\ \left(\dfrac{\partial w_0}{\partial y}\right)^2 \\ 2\dfrac{\partial w_0}{\partial x}\dfrac{\partial w_0}{\partial y} \end{Bmatrix} = 0.5 \underbrace{\begin{bmatrix} \dfrac{\partial w_0}{\partial x} & 0 \\ 0 & \dfrac{\partial w_0}{\partial y} \\ \dfrac{\partial w_0}{\partial y} & \dfrac{\partial w_0}{\partial x} \end{bmatrix}}_{\mathcal{H}} \underbrace{\begin{Bmatrix} \dfrac{\partial w_0}{\partial x} \\ \dfrac{\partial w_0}{\partial y} \end{Bmatrix}}_{\mathfrak{d}} \tag{8}$$

The bending strain $\boldsymbol{\kappa}$ is determined by

$$\boldsymbol{\kappa} = \begin{Bmatrix} \kappa_{xx} \\ \kappa_{yy} \\ \kappa_{xy} \end{Bmatrix} = \begin{Bmatrix} \dfrac{\partial \theta_x}{\partial x} \\ \dfrac{\partial \theta_y}{\partial y} \\ \dfrac{\partial \theta_x}{\partial y} + \dfrac{\partial \theta_y}{\partial x} \end{Bmatrix} \tag{9}$$

The transverse shear strain $\boldsymbol{\gamma}$ in the n-FSDT is defined as:

$$\boldsymbol{\gamma} = \hbar(z) \begin{Bmatrix} \dfrac{\partial w_0}{\partial x} + \theta_x \\ \dfrac{\partial w_0}{\partial y} + \theta_y \end{Bmatrix} \tag{10}$$

where the shear strain distribution function is given by $\hbar(z) = \frac{2\sqrt{5}}{3}\cos^2\left(\frac{\pi z}{h}\right)$. Unlike the constant shear correction factor 5/6 in classical FSDT, this distribution satisfies the physical boundary condition of zero transverse shear stress at the top and bottom surfaces $\left(z = \pm\frac{h}{2}\right)$. Moreover, it ensures that the average transverse shear strain energy is equivalent to that obtained from the classical correction factor, while simultaneously providing a more realistic transverse shear stress distribution consistent with three-dimensional elasticity theory. Therefore, this formulation represents the so-called n-FSDT, which improves the accuracy of the conventional FSDT without increasing the number of kinematic variables.

It should be noted that the proposed shear strain distribution function also approximates the parabolic-type variation of transverse shear stresses predicted by three-dimensional elasticity solutions. In classical FSDT formulations, the assumption of constant transverse shear strain through the thickness leads to unrealistic shear stress distributions and requires an empirical shear correction factor to restore the correct shear energy. In contrast, the present function $\hbar(z)$ introduces a physically consistent thickness-wise variation that automatically satisfies the traction-free boundary conditions at the upper and lower surfaces while maintaining the correct global shear energy. Consequently, the proposed formulation provides a better approximation of the actual transverse shear behavior, particularly for moderately thick plates and sandwich shells where transverse shear effects are significant.

2.4 Constitutive relations

The internal force result is:

$$\begin{Bmatrix} \mathbf{N} \\ \mathbf{M} \end{Bmatrix} = \mathbf{D}_m \begin{Bmatrix} \boldsymbol{\varepsilon}_m^L + \boldsymbol{\varepsilon}_m^{NL} \\ \boldsymbol{\kappa} \end{Bmatrix}; \mathbf{Q} = \mathbf{D}_s \boldsymbol{\gamma} \tag{11}$$

where $\mathbf{N}, \mathbf{M}, \mathbf{Q}$ denote the in-plane force, bending moment, and shear force vectors, respectively.

The stiffness matrices are defined by

$$\mathbf{D}_m = \begin{bmatrix} \mathbb{A} & \mathbb{B} \\ \mathbb{B} & \mathbb{S} \end{bmatrix};\ \mathbf{D}_s = \sum_{i=1}^{3} \int_{h_i}^{h_{i+1}} \frac{E^{(i)}(z)}{2(1+\nu^{(i)}(z))} \begin{bmatrix} 1 & 0 \\ 0 & 1 \end{bmatrix} dz \tag{12}$$

where $\mathbb{A}, \mathbb{B}$, and $\mathbb{S}$ represent the extensional stiffness matrix, the bending–extensional coupling stiffness matrix, and the bending stiffness matrix, respectively:

$$(\mathbb{A}, \mathbb{B}, \mathbb{S}) = \sum_{i=1}^{3} \int_{h_i}^{h_{i+1}} \frac{E^{(i)}(z)}{1-\nu^{(i)}(z)^2} \begin{bmatrix} 1 & \nu^{(i)}(z) & 0 \\ \nu^{(i)}(z) & 1 & 0 \\ 0 & 0 & \dfrac{1}{2/(1-\nu^{(i)}(z))} \end{bmatrix} (1, z, z^2) dz \tag{13}$$

Hence, Eq. (11) can be rewritten in compact form:

$$\begin{Bmatrix} \mathbf{N} \\ \mathbf{M} \\ \mathbf{Q} \end{Bmatrix} = \begin{bmatrix} \mathbb{A} & \mathbb{B} & 0 \\ \mathbb{B} & \mathbb{S} & 0 \\ 0 & 0 & \mathbf{D}_s \end{bmatrix} \begin{Bmatrix} \boldsymbol{\varepsilon}_m^L + \boldsymbol{\varepsilon}_m^{NL} \\ \boldsymbol{\kappa} \\ \boldsymbol{\gamma} \end{Bmatrix} \tag{14}$$

2.5 The governing equation

Applying Hamilton's principle (Reddy, 2003), the governing equation is determined by

$$\int_{t_1}^{t_2} (\delta\mathcal{U} + \delta W - \delta\mathcal{K}) \mathrm{d}t = 0 \tag{15}$$

in which

The strain energy $\mathcal{U}$ is:

$$\mathcal{U} = \frac{1}{2} \int_S (\boldsymbol{\varepsilon}^T \boldsymbol{D}_m \boldsymbol{\varepsilon} + \boldsymbol{\gamma}^T \boldsymbol{D}_s \boldsymbol{\gamma}) \mathrm{d}S \tag{16}$$

The work done of the external load W is:

$$W = \int_S q(x, y, t) w_0 \mathrm{d}S \tag{17}$$

The kinetic energy $\mathcal{K}$ is:

$$\mathcal{K} = \frac{1}{2} \int_S \dot{\boldsymbol{u}}^T \boldsymbol{m} \dot{\boldsymbol{u}} \mathrm{d}S \tag{18}$$

with generalized displacement vector $\boldsymbol{u}$ and inertial matrix $\boldsymbol{m}$ are determined by

$$\boldsymbol{u}^T = \{u_0 \quad v_0 \quad w \quad \theta_x \quad \theta_y\} \tag{19a}$$

$$\boldsymbol{m} = \begin{bmatrix} m_1 & 0 & 0 & m_2 & 0 \\ & m_1 & 0 & 0 & m_2 \\ & & m_1 & 0 & 0 \\ & & & m_3 & 0 \\ sym & & & & m_3 \end{bmatrix} \tag{19b}$$

where $(m_1, m_2, m_3) = \sum_{i=1}^{3} \int_{h_i}^{h_{i+1}} \rho^{(i)}(z)\,(1, z, z^2) \mathrm{d}z$.

By substituting Eqs. (16-18) into Eq. (15), the weak form governing the vibration analysis of shells can be formally expressed as follows:

$$\int_S \delta\boldsymbol{\varepsilon}^T \boldsymbol{D}_m \boldsymbol{\varepsilon} \mathrm{d}S + \int_S \delta\boldsymbol{\gamma}^T \boldsymbol{D}_s \boldsymbol{\gamma} \mathrm{d}S + \int_S q(x, y, t) \delta w_0 \mathrm{d}S = \int_S \dot{\boldsymbol{u}}^T \boldsymbol{m} \dot{\boldsymbol{u}} \mathrm{d}S \tag{20}$$

2.6 Finite element procedure

For the Q4 element, the nodal displacement vector is (Reddy, 2003):

$$\mathbf{q} = \{q_1^T \quad q_2^T \quad q_3^T \quad q_4^T\}^T \tag{21}$$

with nodal degrees of freedom:

$$q_i = \begin{Bmatrix} u_{0i} \\ v_{0i} \\ w_{0i} \\ \varphi_{xi} \\ \varphi_{yi} \end{Bmatrix}, i = 1, \dots, 4 \tag{22}$$

The nonlinear motion equation of shells can be defined by (Reddy, 2000):

$$\boldsymbol{M}\ddot{\boldsymbol{q}} + \boldsymbol{C}\dot{\boldsymbol{q}} + (\boldsymbol{K}_L + \boldsymbol{K}_{NL} + \boldsymbol{K}_G)\boldsymbol{q} = \boldsymbol{F}(t) \tag{23}$$

where $\boldsymbol{K}_L = \sum_1^{ne} \boldsymbol{K}_L^e$, $\boldsymbol{K}_{NL} = \sum_1^{ne} \boldsymbol{K}_{NL}^e$, and $\boldsymbol{K}_G = \sum_1^{ne} \boldsymbol{K}_G^e$ denote the global linear stiffness matrix, nonlinear stiffness matrix, and geometric stiffness matrix, respectively. The global mass matrix is given by $\boldsymbol{M} = \sum_1^{ne} \boldsymbol{M}^e$, and the global load vector is defined as $\boldsymbol{F}(t) = \sum_1^{ne} \boldsymbol{F}^e(t)$, where ne is the total of elements. $\boldsymbol{C}$ is synthesized from the mass matrix $\boldsymbol{M}$ and the linear stiffness matrix $\boldsymbol{K}_L$ through the damping ratio ζ and the first two frequencies ω_1 and ω_2 (Reddy, 2015).

The element linear stiffness matrix is:

$$\boldsymbol{K}_L^e = \mathbb{T}_e \left(\int_{S_e} (\mathbf{B}^L)^T \tilde{\mathbb{C}} \mathbf{B}^L \, \mathrm{d}S \right) \mathbb{T}'_e \, ; \tag{24}$$

The element nonlinear stiffness matrix is:

$$\boldsymbol{K}_{NL}^e = \mathbb{T}_e \left(\int_{S_e} \left(\frac{1}{2} (\mathbf{B}^L)^T \tilde{\mathbb{C}} \mathbf{B}^{NL} + (\mathbf{B}^{NL})^T \tilde{\mathbb{C}} \mathbf{B}^L + \frac{1}{2} \int_{S_e} (\mathbf{B}^{NL})^T \tilde{\mathbb{C}} \mathbf{B}^{NL} \right) \mathrm{d}S \right) \mathbb{T}'_e \tag{25}$$

in which

$$\tilde{\mathbb{C}} = \begin{bmatrix} \boldsymbol{D}_m & \mathbf{0} \\ \mathbf{0} & \boldsymbol{D}_s \end{bmatrix}; \; \mathbf{B}^L = [\mathcal{B}^{0L} \quad \mathcal{B}^b \quad \mathcal{B}^s]^T; \; \mathbf{B}^{NL} = [\mathcal{B}^{0NL} \quad \mathbf{0}]^T; \tag{26a}$$

$$\mathbf{B}^{0NL} = \boldsymbol{\mathcal{H}} \overline{\mho} \text{ with } \overline{\mho} = \sum_{i=1}^{4} \begin{bmatrix} 0 & 0 & N_{i,x} & 0 & 0 \\ 0 & 0 & N_{i,y} & 0 & 0 \end{bmatrix} \tag{26b}$$

The strain–displacement matrices $\mathcal{B}^{0L}$, $\mathcal{B}^b$, and $\mathcal{B}^s$ are listed in Dvorkin and Bathe (1984). $\mathbb{T}_e$ represents the transformation from the local coordinate system ($O'x'y'z'$) of the flat element to the global coordinate system ($Oxyz$).

The element geometry stiffness matrix is:

$$\boldsymbol{K}_G^e = \mathbb{T}_e \left(\int_{S_e} (\overline{\mho})^T \, \mathbb{R} \, \overline{\mho} \mathrm{d}S \right) \mathbb{T}'_e; \tag{27}$$

where

$$\mathbb{R} = \begin{bmatrix} N_x & N_{xy} \\ N_{xy} & N_y \end{bmatrix} \text{ with } \left(N_x, N_y, N_{xy} \right) = \int_{-\mathrm{h}/2}^{\mathrm{h}/2} \left(\sigma_x, \sigma_y, \sigma_{xy} \right) dz \tag{28}$$

The element mass matrix is:

$$\boldsymbol{M}^e = \mathbb{T}_e \left(\int_{S_e} \mathbb{N}^T \boldsymbol{m} \mathbb{N} \, \mathrm{d}S \right) \mathbb{T}'_e; \tag{29}$$

in which

$$\mathbb{N} = \sum_{i=1}^{4} \begin{bmatrix} N_i & 0 & 0 & 0 & 0 \\ & N_i & 0 & 0 & 0 \\ & & N_i & 0 & 0 \\ & & & N_i & 0 \\ \text{sym} & & & & N_i \end{bmatrix}; \tag{30}$$

with $N_i(r, s)$ is Lagrange shape functions in the natural coordinate system (r, s) (Reddy, 2003).

The element loading vector is:

$$\boldsymbol{F} = \left(\int_{S_e} \mathbb{N}_w^T \, p(t) dS \right) \mathbb{T}'_e; \tag{31}$$

where $\mathbb{N}_w$ is expressed by

$$\mathbb{N}_w = \sum_{i=1}^{4} \{0 \quad 0 \quad N_i \quad 0 \quad 0\}. \tag{32}$$

After imposing the boundary conditions listed in Table 1, Eq. (21) is numerically integrated using the Newmark-β method in conjunction with the Newton–Raphson iterative algorithm (Reddy, 2015).

The EBCs are implemented by attaching elastic springs with finite stiffness k to the corresponding degrees of freedom (DOFs) in the finite element model. The stiffness of these springs is incorporated into the global stiffness matrix as additional diagonal terms, which constrain the boundary displacements proportionally to the assigned stiffness k. This

modeling technique enables a smooth transition between boundary types: $k \to \infty$ corresponds to Dirichlet boundary; $k = 0$ represents the free condition; and finite k values simulate semi-rigid or elastic supports. Therefore, the EBC formulation provides a unified and flexible framework for simulating a wide range of practical BCs in sandwich structures. The stiffness values of the boundary springs are selected based on the relative stiffness between the elastic supports and the FG sandwich shell. Considering that the ceramic core (Si3N4) and the metallic constituent (SUS304) exhibit high elastic moduli, very large spring stiffness values (10^{14}) are used to approximate Dirichlet boundary, whereas finite stiffness values (10^{9}) are employed to simulate elastic supports.

Table 1 Boundary conditions at edges 1 and 2 of shells.

Boundary type	At edge i $(i = 1,2)$
Simply supported (SS)	$k_v(i) = k_w(i) = 10^{14}\text{N/m};\ k_{\theta y}(i) = 10^{14}\text{Nm/rad}$
Clamped (CC)	$k_u(i) = k_v(i) = k_w(i) = 10^{14}\text{N/m};k_{\theta x}(i) = k_{\theta y}(i) = 10^{14}\text{Nm/rad}$
Elastic simply supported (E-SS)	$k_v(i) = k_w(i) = 10^{9}\text{N/m};\ k_{\theta y}(i) = 10^{9}\text{Nm/rad}$
Elastic clamped (E-CC)	$k_u(i) = k_v(i) = k_w(i) = 10^{9}\text{N/m};\ k_{\theta x}(i) = k_{\theta y}(i) = 10^{9}\text{Nm/rad}$

3 NUMERICAL RESULTS

In this section, numerical simulations are conducted to verify the accuracy and efficiency of the proposed formulation, followed by a comprehensive parametric investigation. The verification examples are performed by comparing the present results with available benchmark solutions reported in the literature, thereby demonstrating the reliability and robustness of the developed finite element model. Subsequently, extensive numerical analyses are carried out to explore the influence of various input parameters–including the gradient index, geometrical ratios, and boundary stiffness–on the dynamic response of FGhCS shells with EBCs subjected to EL. The material properties of the constituent layers used in all simulations are summarized in Table 2.

Table 2 The mechanical properties of component materials.

Materials	Elastic modulus (GPa)	Density (kg/m3)	Poisson's ratio
SUS304 (metal)	201.04	8166	0.3
Si3N4 (ceramic)	348.43	2370	0.3

3.1. Verification

Firstly, to validate the accuracy of the proposed cylindrical shell formulation under various BCs, the dimensionless frequency parameter $\bar{\omega} = \omega R\sqrt{\frac{(1-\nu_s^2)\rho}{E}}$ of an isotropic and homogeneous cylindrical shell is compared with the benchmark results reported by Loy et al. (1997). The reference shell is analyzed under several boundary conditions, including SS, CS (clamped- simply supported), and CC at the two circumferential edges, with the geometric parameters $L/R = 20$, $h/R = 0.01$, and $R = 1$. The adopted material properties are $\rho = 7850\,\text{kg/m}^3$, $E = 200\,\text{GPa}$, and $\nu = 0.3$. The present results obtained using the MITC4 element based on the proposed n-FSDT show better agreement than those obtained using the conventional MITC4–FSDT formulation. Moreover, they exhibit excellent agreement with the results reported by Loy et al. (1997), who employed classical shell theory in conjunction with the generalized differential quadrature (GDQ) method, as shown in Table 3. Note that the superscripts "*" and "**" respectively represent the MITC4 results based on classical FSDT and n-FSDT, respectively.

Next, supplementary analyses were conducted using ANSYS Mechanical APDL 2021 R2 with the SHELL181 element, which is a four-node shell element possessing six DOFs per node. The cylindrical shell was discretized using 40 elements along the circumferential direction and 200 elements along the axial direction to ensure mesh convergence. The results obtained from ANSYS are nearly identical to those of the proposed MITC4-based formulation and the reference data by Loy et al. (1997) as summarized in Table 4. These findings demonstrate the reliability and precision of the developed model in capturing the free vibration of cylindrical shells.

Finally, a fully simply supported (SSSS) isotropic rectangular plate is considered. The plate dimensions are $a = b = 2.438\,\text{m}$ and $h = 6.35\,\text{mm}$, while the material properties are $E = 70\text{GPa}$, $\rho = 2547\text{kg/m}^3$, and $\nu = 0.25$. The plate is subjected to a suddenly applied constant uniform pressure $p(t) = 48.82\text{Pa}$ at $t = 0$, which lasts for 0.2s. The nonlinear central deflection response obtained from the present finite element formulation is compared with the benchmark

results of Shen et al. (2019) employing the quadrature element method. As depicted in Figure 3, the present results exhibit excellent agreement with the reference data, both in terms of the peak deflection and the overall transient response trend. This close correspondence demonstrates the accuracy, robustness, and numerical stability of the developed formulation in capturing the nonlinear dynamic behavior. The successful validation against the results of QEM further confirms the reliability of the proposed method.

Table 3 Comparison of fundamental frequencies ($\bar{\omega}$) of isotropic cylindrical shells via BCs.

Modes	Boundary conditions					
	SS		SC		CC	
	Present	Loy et al. (1997)	Present	Loy et al. (1997)	Present	Loy et al. (1997)
1	0.01621* 0.01625**	0.016101	0.02419* 0.02422**	0.023974	0.033112* 0.033116**	0.032885
2	0.01102* 0.01112**	0.009382	0.01202* 0.01208**	0.011225	0.141024* 0.141027**	0.013932
3	0.02313* 0.02318**	0.022105	0.02313* 0.02316**	0.02231	0.02316* 0.02319**	0.022672
4	0.04376* 0.04380**	0.042095	0.04322* 0.04327**	0.042139	0.043125* 0.043128**	0.042208

Table 4 Comparison of fundamental frequency ($\bar{\omega}$) of isotropic cylindrical shells with ANSYS software.

Modes	ANSYS (shell181) SS	ANSYS (shell181) CC	Loy et al. (1997) SS/CC	MITC4 SS/CC
1	0.01622	0.03311	0.01610/0.03289	0.01621/0.03311
2	0.01101	0.01410	0.00938/0.01393	0.01102/0.01410
3	0.02313	0.02316	0.02211/0.02267	0.02313/0.02316
4	0.04377	0.04313	0.04210/0.04221	0.04376/0.04312

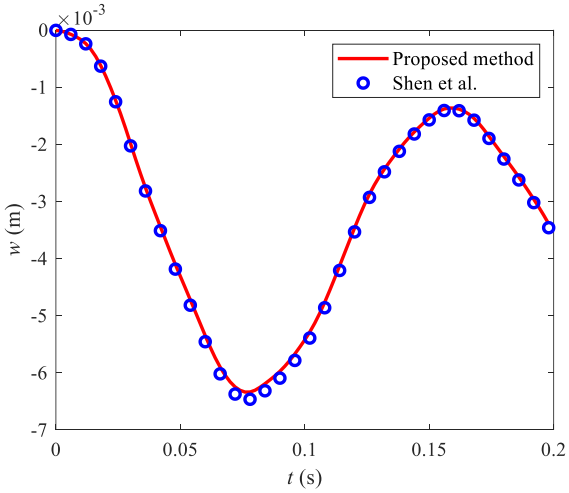

Figure 3 The nonlinear center deflection response of the plate.

3.2. Free vibration problem

Figure 4 illustrates the first six mode shapes of the E–CC FGhCS shell, providing fundamental insights into its vibration behavior governed by the nonuniform material distribution. The variation of stiffness and the shift of the neutral surface through the thickness strongly influence the deformation mechanisms. The lower modes are primarily dominated by global bending and overall ovalization, reflecting the structural flexibility of the shell, whereas the higher modes reveal more localized, intricate deformation patterns associated with shear and circumferential distortions. The inherent material asymmetry introduced by the functional gradation leads to a discernible deviation of the mode shapes compared with those of homogeneous counterparts, highlighting the coupling between extensional and bending responses.

Table 5 summarizes the evolution of the fundamental frequencies of FGhCS shells with variations in the material properties and geometric parameters. A clear and monotonic decrease in frequency is observed with increasing power-law index n. This trend reflects the intrinsic softening effect induced by the gradation: as n increases, the ceramic volume fraction decreases while the metal-rich content dominates, resulting in a lower effective modulus and enhanced overall rigidity. Consequently, the structure exhibits greater resistance to dynamic deformation and stores more vibrational energy per unit displacement. In contrast, an increase in the thickness of the ceramic core–particularly in the 2:1:2, 2:1:1, and 1:2:1 configurations–leads to a pronounced increase in the natural frequencies. The addition of ceramic layers increases the effective stiffness and decreases structural inertia, thus increasing the mass–stiffness ratio and yielding a stiffer dynamic response. Among these configurations, the 2:1:1 arrangement stands out due to its asymmetric layering, which induces a strong flexural–membrane coupling. This coupling modifies the modal characteristics and redistributes the vibration modes compared with symmetric configurations. Such asymmetry-driven coupling plays a crucial role in realistic FGM sandwich structures and must be explicitly considered in predictive vibration models for hierarchical composites.

The geometric parameter L/R (length-to-radius ratio) further governs the dynamic stiffness. Shells with larger L/R ratios exhibit reduced lateral rigidity, making them more susceptible to low-frequency global oscillations, especially under elastic boundary supports. Conversely, Dirichlet-type boundaries restrict both translational and rotational motion, thereby elevating the natural frequencies. The observed frequency reduction under elastic supports arises from partial edge compliance, which allows localized energy dissipation and modal concentration near the boundaries.

Generally, these results underscore the intricate coupling among material gradation, geometric parameters, and boundary flexibility in governing the free vibration of FGhCS shells. Accurate incorporation of these coupled effects is essential for high-fidelity modeling and for optimizing the dynamic performance of lightweight aerospace, marine, and multifunctional energy-harvesting structures, where stiffness-to-weight and damping-to-frequency ratios are critical design metrics.

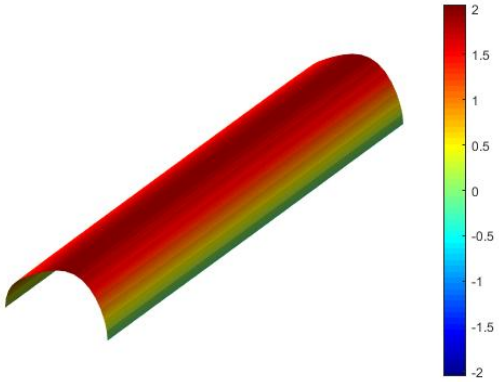

1st mode, $f_1 = 62.2910$ Hz

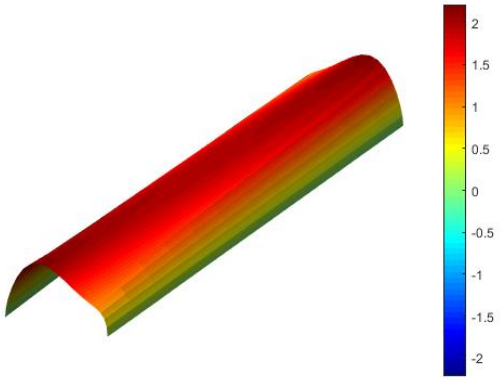

2nd mode, $f_2 = 69.3038$ Hz

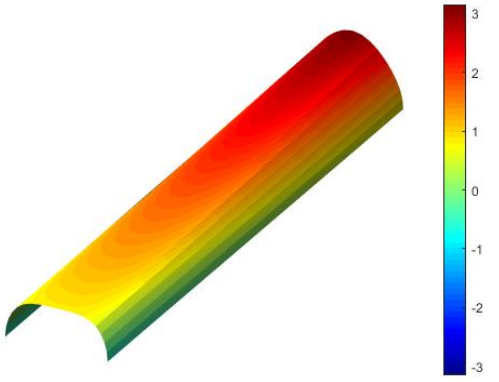

3rd mode, $f_3 = 72.2842$ Hz

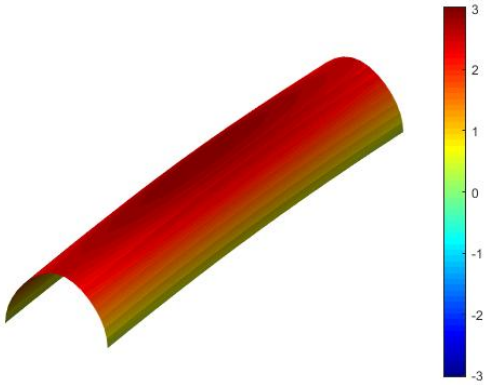

4th mode, $f_4 = 72.8752$ Hz

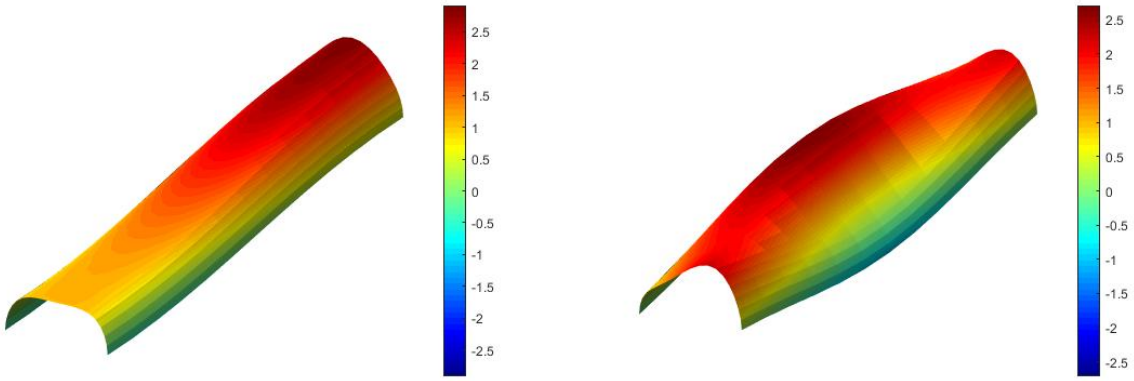

5th mode, $f_5 = 86.8737$ Hz 6th mode, $f_6 = 96.3240$ Hz

Figure 4 The first six mode shapes of the E-CC FGhCS shell (1:2:1) with $R = 2$ m, $L = 10R, h = R/10,\ n = 1$.

Table 5 The fundamental frequencies of FGhCS shell with $R = 2$ m and $h = R/15$.

BCs	Thickness ratio	*n*	The fundamental frequency (Hz)					
			$L/R = 8$	10	12	14	16	18
E-SS	2:1:2		84.1386	78.7038	74.0749	70.0916	66.6269	63.5833
			55.056	52.1387	49.5526	47.2535	45.2002	43.3568
			49.6357	47.1724	44.9642	42.9821	41.1973	39.5839
			46.225	44.0249	42.0393	40.2466	38.6242	37.1511
			44.1296	42.0729	40.2107	38.5246	36.9947	35.6026
	2:1:1		84.1386	78.7038	74.0749	70.0916	66.6269	63.5833
			56.1585	53.1607	50.5075	48.1518	46.0502	44.1651
			50.8285	48.2767	45.9942	43.9494	42.111	40.4513
			47.4615	45.1691	43.1057	41.2472	39.5684	38.0467
			45.3979	43.247	41.3051	39.5512	37.9634	36.5211
	1:2:1		84.1386	78.7038	74.0749	70.0916	66.6269	63.5833
			62.545	59.0365	55.959	53.2472	50.8431	48.6982
			57.749	54.6692	51.9422	49.5204	47.3594	45.4208
			54.538	51.7361	49.2389	47.0089	45.0095	43.2087
			52.5099	49.8748	47.5169	45.4041	43.5043	41.789
E-CC	2:1:2		88.69	82.4012	77.148	72.6975	68.8753	65.5525
			58.65	55.1652	52.1304	49.4747	47.1356	45.0611
			53.0271	50.0613	47.4463	45.1347	43.0817	41.2485
			49.4649	46.8042	44.4405	42.3379	40.4607	38.7772
			47.2575	44.7653	42.5433	40.5604	38.7854	37.1901
	2:1:1		88.69	82.4012	77.148	72.6975	68.8753	65.5525
			59.8146	56.2373	53.1268	50.4084	48.0164	45.8966
			54.2883	51.22	48.521	46.1396	44.0278	42.1445
			50.773	48.005	45.553	43.3769	41.4378	39.7015
			48.5997	45.9977	43.6848	41.6263	39.7875	38.1377
	1:2:1		88.69	82.4012	77.148	72.6975	68.8753	65.5525
			66.4495	62.291	58.7103	55.6055	52.8907	50.4971
			61.5047	57.8283	54.6307	51.8357	49.376	47.1961
			58.1837	54.8231	51.8791	49.2908	47.0022	44.9661
			56.0769	52.9075	50.1189	47.6582	45.476	43.5299
SS	2:1:2		117.7969	117.8514	117.8847	117.9069	117.9227	117.9344
			70.8173	70.8484	70.8675	70.8801	70.8892	70.8958
			62.5219	62.5492	62.5658	62.5769	62.5848	62.5906
			57.5287	57.5538	57.5691	57.5793	57.5866	57.5919
			54.6086	54.6325	54.6472	54.6569	54.6639	54.669

	2:1:1	117.7969	117.8514	117.8847	117.9069	117.9227	117.9344
		72.4418	72.4737	72.4931	72.5061	72.5154	72.5222
		64.2735	64.3015	64.3187	64.3301	64.3382	64.3442
		59.3352	59.3611	59.3769	59.3874	59.3949	59.4004
		56.4514	56.4762	56.4913	56.5014	56.5086	56.5139
	1:2:1	117.7969	117.8514	117.8847	117.9069	117.9227	117.9344
		82.122	82.1583	82.1805	82.1952	82.2058	82.2135
		74.4428	74.4752	74.4951	74.5083	74.5177	74.5246
		69.4346	69.4646	69.483	69.4952	69.5039	69.5103
		66.3626	66.3912	66.4087	66.4203	66.4286	66.4347
CC	2:1:2	129.874	129.9296	129.9639	129.9868	130.0031	130.0152
		78.1332	78.1652	78.1848	78.1979	78.2072	78.2141
		68.9898	69.0177	69.0349	69.0464	69.0546	69.0606
		63.4813	63.507	63.5228	63.5334	63.5409	63.5465
		60.2555	60.2801	60.2951	60.3052	60.3124	60.3178
	2:1:1	129.874	129.9296	129.9639	129.9868	130.0031	130.0152
		79.9291	79.9619	79.9819	79.9954	80.005	80.0121
		70.9293	70.9581	70.9758	70.9876	70.996	71.0023
		65.4834	65.5099	65.5263	65.5372	65.545	65.5507
		62.2986	62.324	62.3396	62.3501	62.3576	62.363
	1:2:1	129.874	129.9296	129.9639	129.9868	130.0031	130.0152
		90.5972	90.6344	90.6572	90.6725	90.6834	90.6915
		82.1391	82.1724	82.1928	82.2065	82.2163	82.2235
		76.6211	76.6518	76.6708	76.6834	76.6925	76.6992
		73.2348	73.2642	73.2822	73.2942	73.3028	73.3092

3.3. Nonlinear dynamic response problem

Figure 5 presents the nonlinear dynamic responses of the E–SS FGhCS shell subjected to EL with various thickness ratios $h_1{:}\,h_2{:}\,h_3$. The results clearly demonstrate a pronounced stiffening effect as the ceramic core layer becomes thicker. Specifically, an increase in the core thickness significantly enhances the overall flexural rigidity of the shell, as observed in the configurations 2:1:2, 1:1:1, 1:2:1, 1:4:1, and 1:8:1. However, a notable deviation from this general trend occurs when the shell is elastically restrained along its longitudinal edges. In this scenario, a higher material stiffness does not necessarily correspond to a smaller overall deflection. As the structure stiffens, the strain energy becomes unevenly distributed, being partially redirected toward the compliant edges. The elastic supports, which allow limited translational and rotational motions, act as flexible energy sinks that deform more noticeably as the stiffened shell core resists bending. Consequently, the ceramic-rich configurations induce larger reaction forces at the boundaries, amplifying local edge displacements and thereby increasing the global deflection (Figure 5(a)), velocity (Figure 5(b)), and normal stress responses (Figure 5(c)). This counterintuitive phenomenon highlights the complex coupling between material gradation and boundary flexibility. Enhanced stiffness modifies the internal energy transmission pathways within the shell, such that ceramic enrichment, while improving rigidity, may simultaneously intensify deformation near elastic supports. Therefore, precise modeling of boundary compliance is essential for the optimal design of FGhCS shells under EL, ensuring a balanced trade-off between stiffness enhancement and deformation control. In addition, the transverse shear stress exhibits a parabolic variation across the thickness and vanishes at both the top and bottom surfaces of the shell (Figure 5(d)). The corresponding phase orbit (Fig.5(f)) forms an open spiral that gradually converges to the equilibrium state due to damping-induced energy dissipation.

Figure 6 illustrates the nonlinear dynamic responses of the SS FGhCS shell subjected to EL for different thickness ratios $h_1{:}\,h_2{:}\,h_3$. Under Dirichlet boundary conditions, an increase in the ceramic-core thickness leads to a substantial enhancement in the overall stiffness of the shell. As the ceramic layer thickens, the bending rigidity of the structure increases correspondingly, effectively constraining deformation and yielding smaller deflection amplitudes. This trend aligns with the expected mechanical behavior, as ceramic-rich configurations possess higher elastic moduli and, consequently, greater resistance to external excitation. The temporal variations of deflection, velocity, and normal stress are presented in Figures 6(a–c), while the corresponding stress distributions through the shell thickness are depicted in Figures 6(d, e). The phase orbit shown in Figure 6(f) exhibits a gradually converging spiral pattern, indicating a stable damped dynamic response.

Figure 7 presents the nonlinear dynamic responses of the E–CC FGhCS shell subjected to EL for various power-law indices n. The results reveal that the power-law index exerts a decisive influence on the stiffness and deformation characteristics of the functionally graded shell. As n increases, the ceramic volume fraction decreases while the metallic constituent becomes more dominant, resulting in a significant reduction in the effective elastic modulus and bending rigidity. Consequently, the shell exhibits greater compliance, leading to larger deflection amplitudes and broader phase orbits under identical excitation conditions. Conversely, smaller values of n correspond to ceramic-rich configurations with higher stiffness, which effectively suppress nonlinear deformation and facilitate faster vibration recovery. When the longitudinal edges are elastically constrained, this material-dependent behavior becomes even more pronounced. The softening effect associated with larger n values allows a greater portion of strain energy to be absorbed by the compliant boundaries, intensifying local edge deformation and amplifying the overall deflection, as shown in Figure 7(a). This finding underscores the strong coupling between material gradation and boundary flexibility, where reduced stiffness due to increased metallic content magnifies the role of elastic edge compliance in shaping the global dynamic response. The corresponding velocity and normal stress evolutions are displayed in Figures 7(b–c), while the through-thickness stress distributions are depicted in Figures 7(d–e) and the phase orbit shown in Figures 7(f). Conversely, under Dirichlet boundary conditions (Figure 8), lateral motion is effectively restrained, and increasing the power-law index n consistently results in larger deflection amplitudes due to the reduced load-bearing capacity of the shell. This behavior reflects the pronounced influence of the power-law index on the shell's mechanical response, where the dominance of the metallic phase at higher n values leads to a softer and more deformable structure. Overall, these results confirm that the power-law index n governs the fundamental trade-off between stiffness and flexibility in FGhCS shells. A higher n enhances deformability and energy absorption but compromises structural stability, whereas a lower n improves rigidity at the expense of increased brittleness. Therefore, precise tailoring of the gradation profile is crucial to achieve an optimal balance between mechanical strength and flexibility, ensuring reliable dynamic performance of FGM-based shell structures under realistic boundary and loading conditions.

Finally, Figures 9 and 10 illustrate the influence of the geometric slenderness ratio L/R on the nonlinear dynamic behavior of the FGhCS shell. The results demonstrate that L/R plays a decisive role in governing both the effective stiffness and the overall deformation characteristics of the structure. As L/R increases, the shell becomes thinner relative to its curvature radius, leading to a pronounced reduction in effective bending stiffness and global stability. Consequently, the shell exhibits larger deflection amplitudes and stronger nonlinear responses under identical loading conditions. This tendency is clearly observed in Figures 9(a)–10(a), where shells with higher L/R ratios experience amplified displacements and slower vibration recovery. From a physical standpoint, an increase in L/R reduces the curvature-induced membrane restraint, rendering the shell more susceptible to bending deformation and dynamic instability. The associated reduction in geometric stiffness weakens the coupling between membrane and bending modes, thereby allowing greater mid-surface stretching and larger out-of-plane deflections. Conversely, shells with smaller L/R ratios exhibit higher curvature and stronger in-plane constraints, which enhance their load-carrying capacity and effectively suppress large-amplitude vibrations. These findings confirm that the geometric slenderness ratio L/R fundamentally governs the stiffness–stability balance of FGhCS shells and must be judiciously optimized during the design phase to ensure desirable dynamic performance and structural reliability.

In the above examples, the damping ratio is chosen as $\zeta = 0.1$. The normal stress σ_{xx} presented in the numerical results is evaluated from the constitutive relations based on the strain field obtained from the finite element solution. Since the present formulation employs flat four-noded MITC4 elements, the stress components are computed in an approximate manner at selected sampling locations within each element. In this study, the stresses are evaluated at quarter-point locations to improve numerical stability and reduce spurious oscillations that may arise from direct nodal stress evaluation. It should be noted that these stresses represent an approximate distribution intended to illustrate the overall stress variation through the structure rather than highly localized stress concentrations.

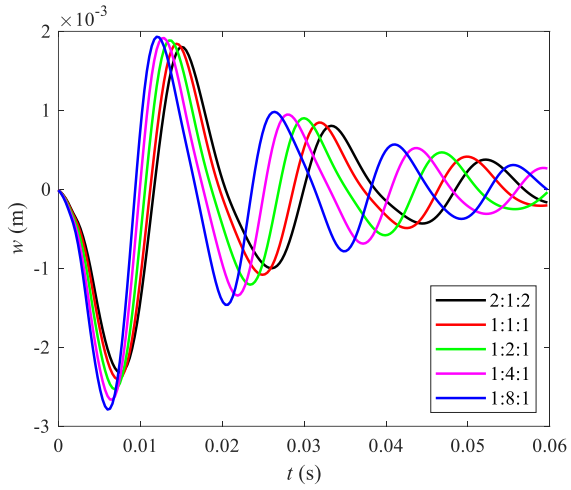

a) The nonlinear centre deflection response

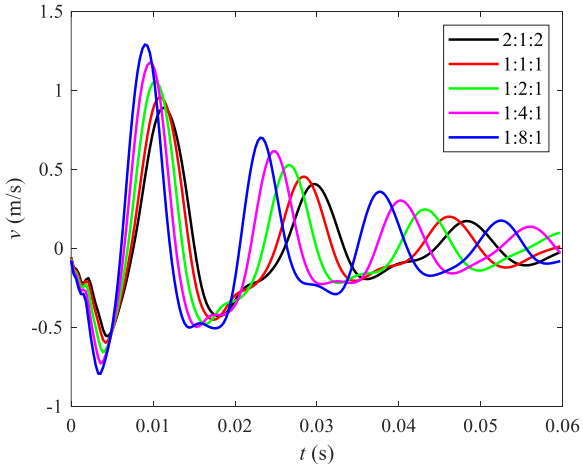

b) The nonlinear centre velocity response

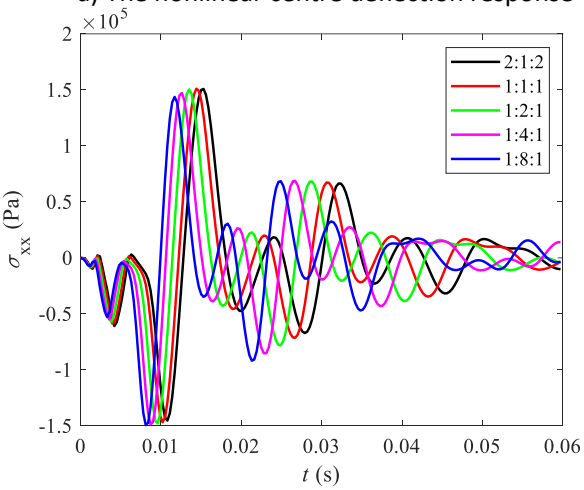

c) The nonlinear stress response $\sigma_{xx}(\frac{a}{2},\frac{b}{2},\frac{h}{2})$

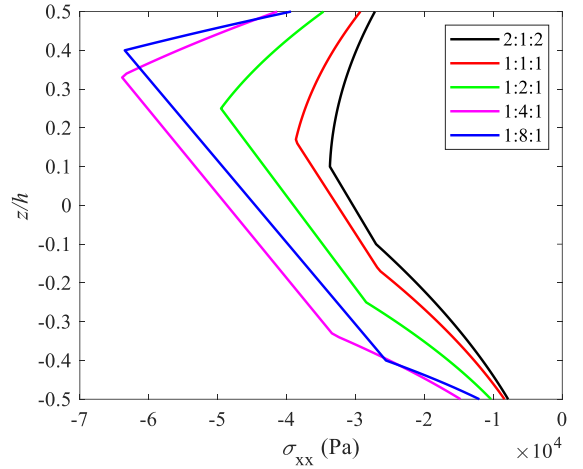

d) The normal stress $\sigma_{xx}(\frac{a}{2},\frac{b}{2},z)$ at the peak-point

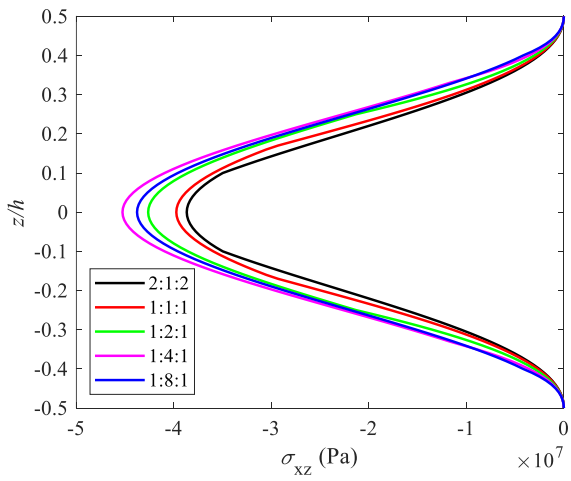

e) The shear stress $\sigma_{xz}(0,\frac{b}{2},z)$ at the peak-point

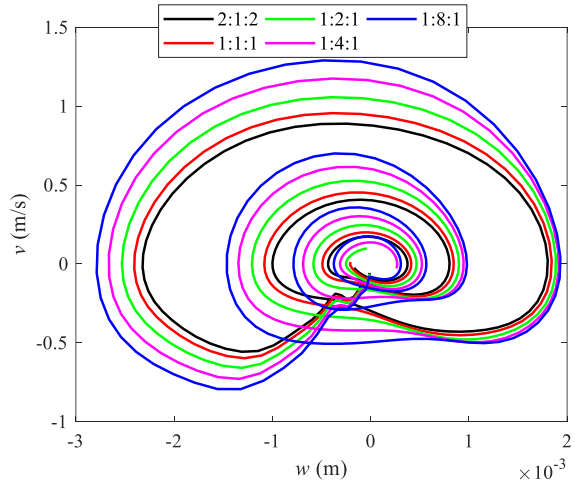

f) Phase orbit (2D-view)

Figure 5 The nonlinear response of E-SS FGhCS shells under EL versus thickness ratio with $R = 2$ m, $L = 10R$, $h = R/10$, and $n = 1$.

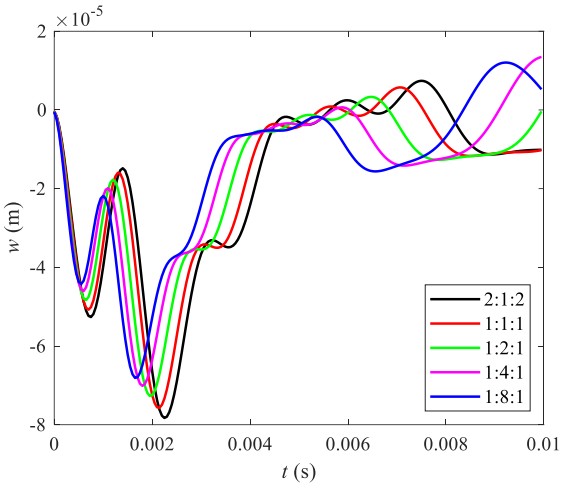

a) The nonlinear centre deflection response

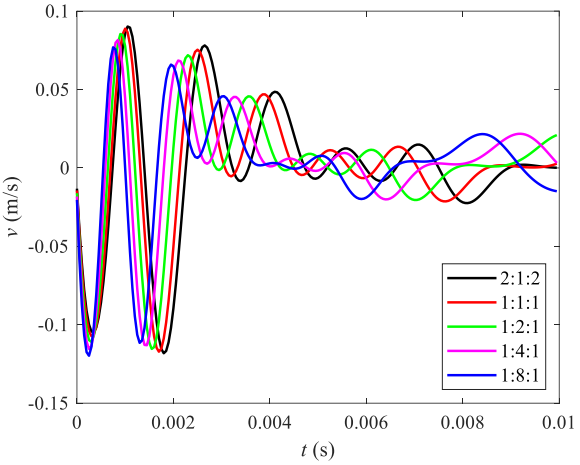

b) The nonlinear centre velocity response

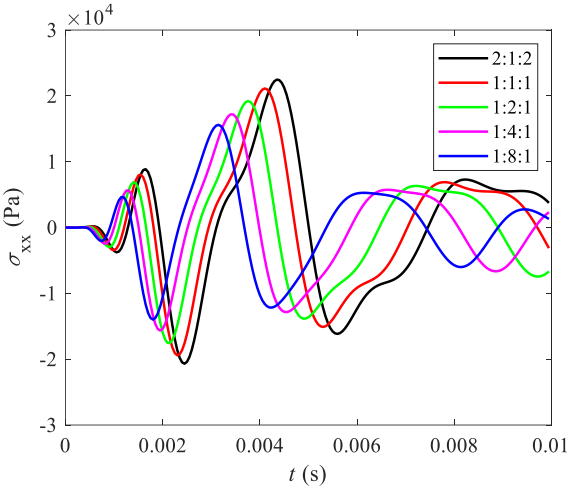

c) The nonlinear stress response $\sigma_{xx}(\frac{a}{2},\frac{b}{2},\frac{h}{2})$

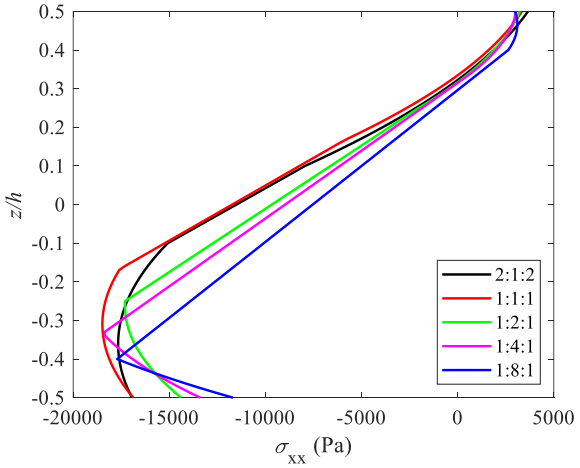

d) The normal stress $\sigma_{xx}(\frac{a}{2},\frac{b}{2},z)$ at the peak-point

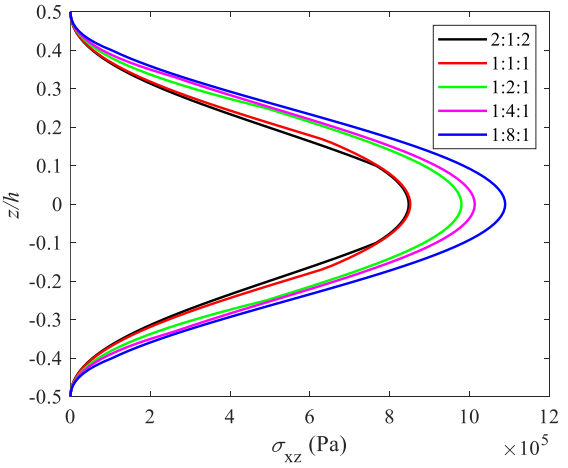

e) The shear stress $\sigma_{xz}(0,\frac{b}{2},z)$ at the peak-point

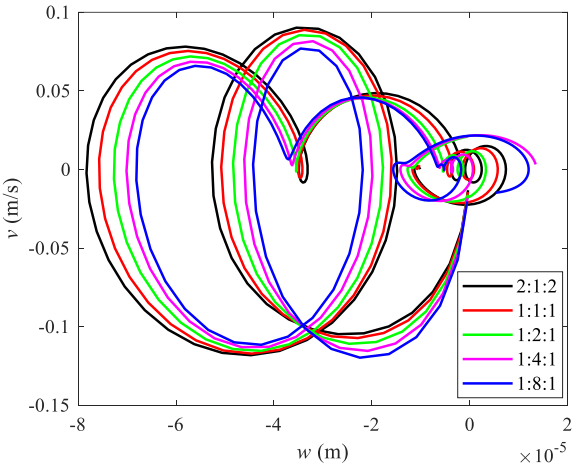

f) Phase orbit (2D-view)

Figure 6 The nonlinear response of SS FGhCS shells under EL versus thickness ratio with $R = 2$ m, $L = 10R$, $h = R/10$, and $n = 1$.

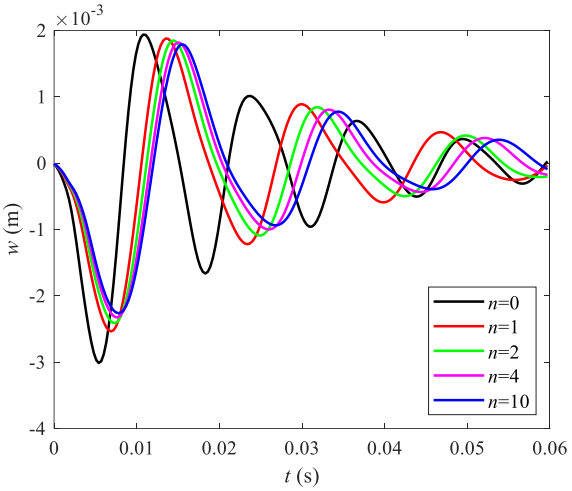

a) The nonlinear centre deflection response

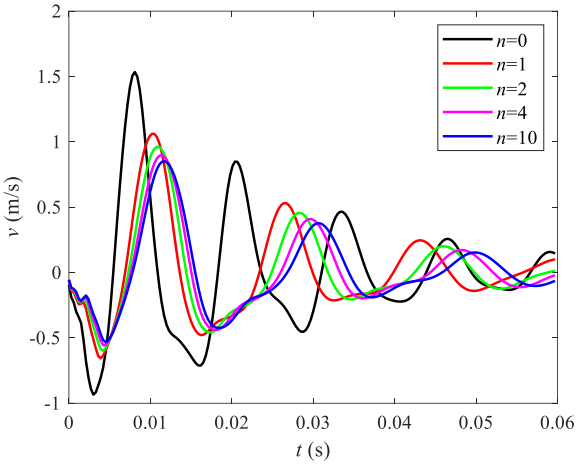

b) The nonlinear centre velocity response

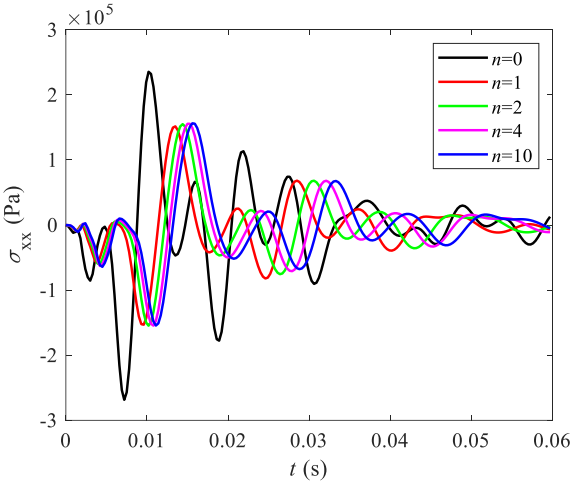

c) The nonlinear stress response $\sigma_{xx}(\frac{a}{2},\frac{b}{2},\frac{h}{2})$

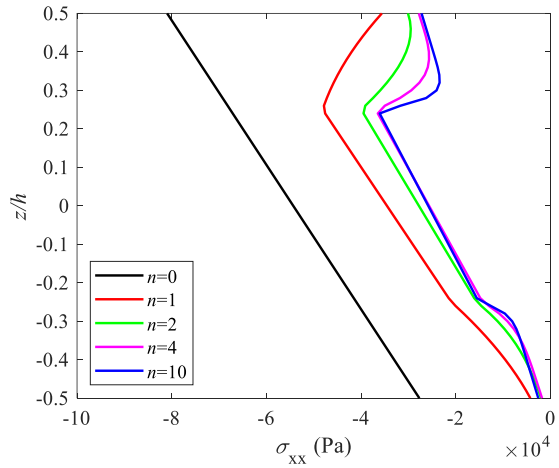

d) The normal stress $\sigma_{xx}(\frac{a}{2},\frac{b}{2},z)$ at the peak-point

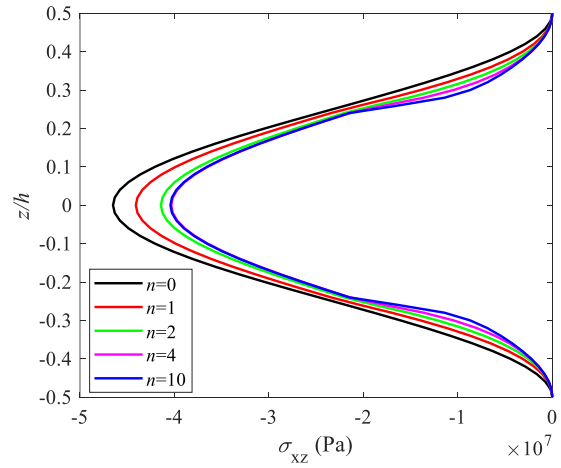

e) The shear stress $\sigma_{xz}(0,\frac{b}{2},z)$ at the peak-point

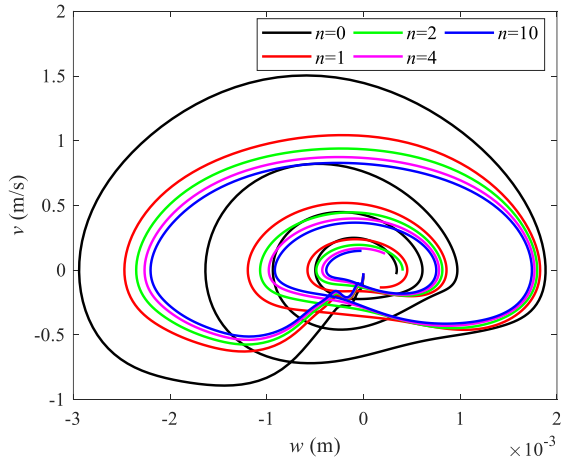

f) Phase orbit (2D-view)

Figure 7 The nonlinear response of E-CC FGhCS shells (1:2:1) under EL versus n with $R = 2$ m, $L = 10R, h = R/10$, and $n = 1$.

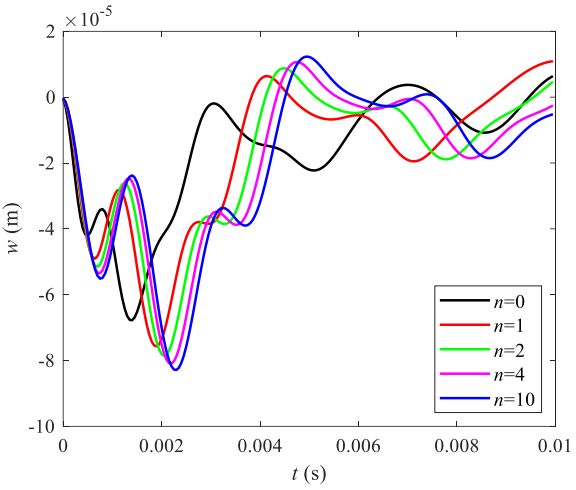

a) The nonlinear centre deflection response

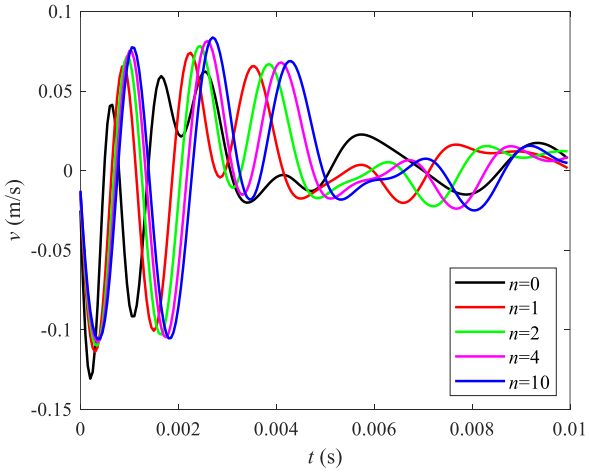

b) The nonlinear centre velocity response

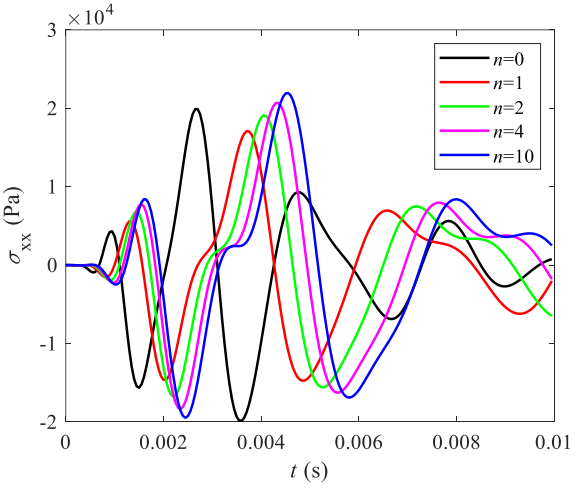

c) The nonlinear stress response $\sigma_{xx}(\frac{a}{2},\frac{b}{2},\frac{h}{2})$

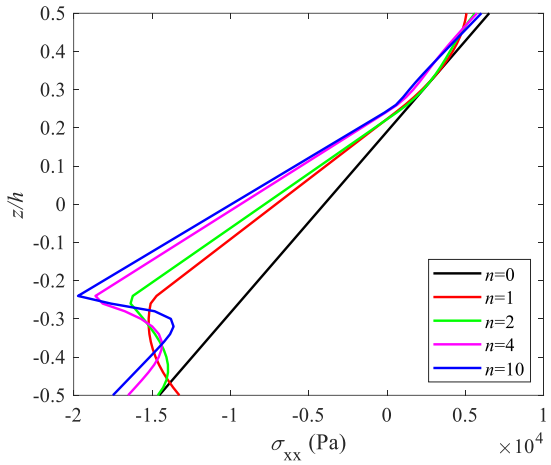

d) The normal stress $\sigma_{xx}(\frac{a}{2},\frac{b}{2},z)$ at the peak-point

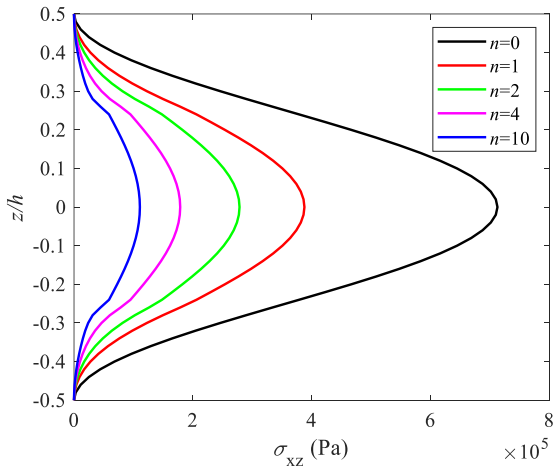

e) The shear stress $\sigma_{xz}(0,\frac{b}{2},z)$ at the peak-point

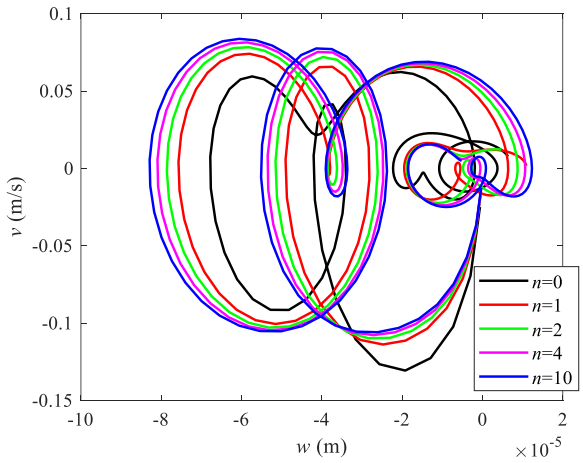

f) Phase orbit (2D-view)

Figure 8 The nonlinear response of CC FGhCS shells (1:2:1) under EL versus n with $R = 2$ m, $L = 10R$, $h = R/10$, and $n = 1$.

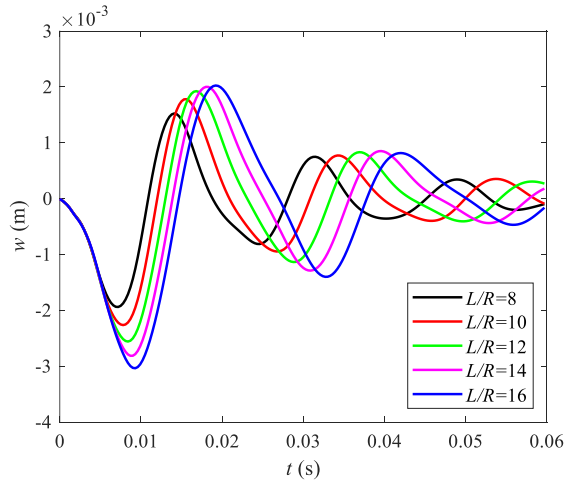

a) The nonlinear centre deflection response

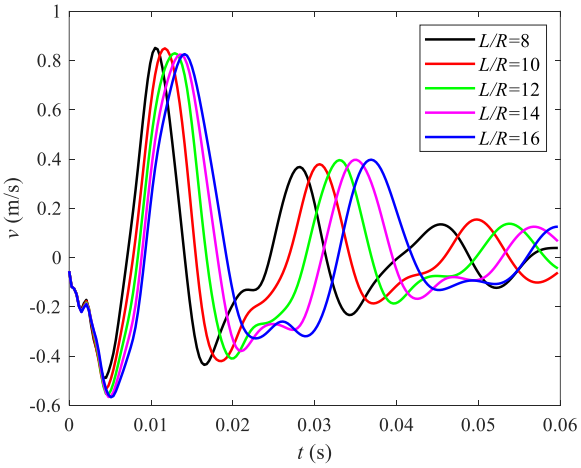

b) The nonlinear centre velocity response

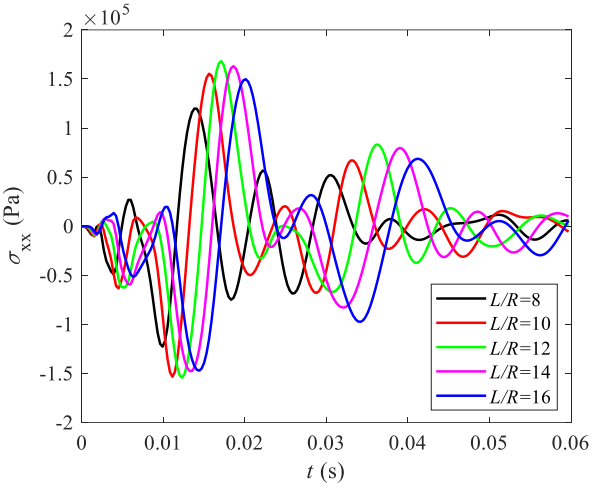

c) The nonlinear stress response $\sigma_{xx}(\frac{a}{2},\frac{b}{2},\frac{h}{2})$

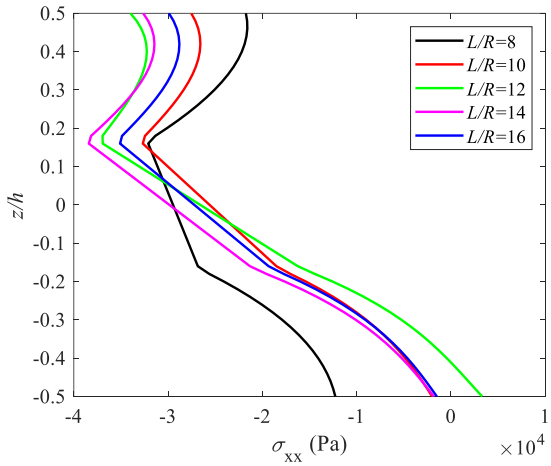

d) The normal stress $\sigma_{xx}(\frac{a}{2},\frac{b}{2},z)$ at the peak-point

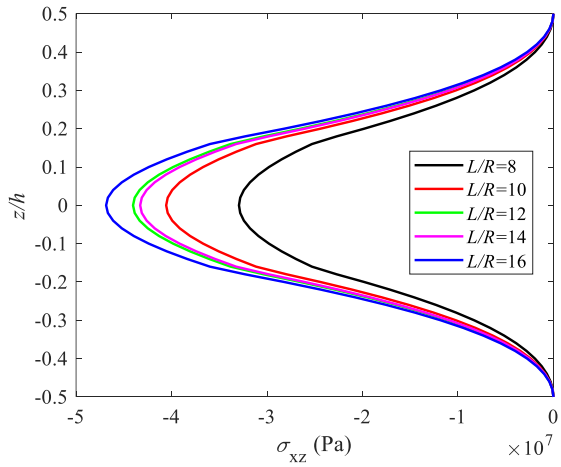

e) The shear stress $\sigma_{xz}(0,\frac{b}{2},z)$ at the peak-point

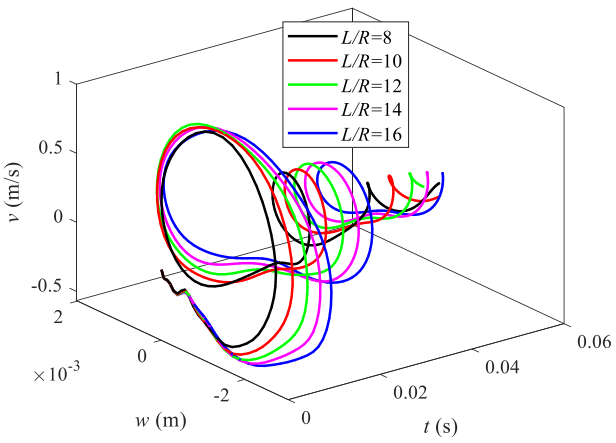

f) Phase orbit (3D-view)

Figure 9 The nonlinear response of E-CC FGhCS shells (1:1:1) under EL versus L/R ratio with $R = 2$ m, $L = 10R$, $h = R/10$, and $n = 2$.

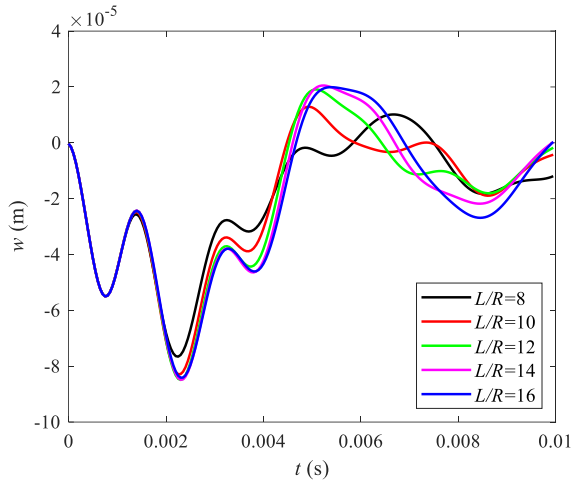

a) The nonlinear centre deflection response

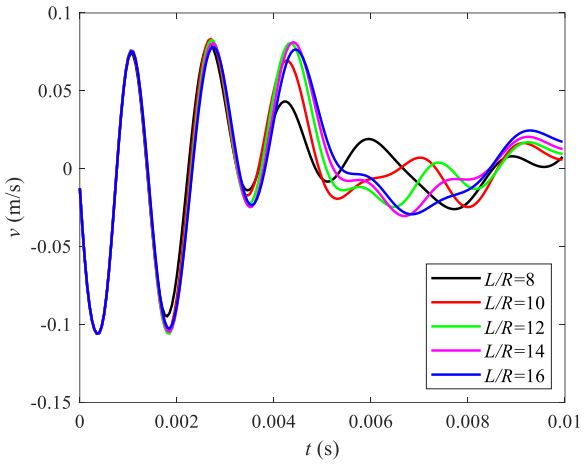

b) The nonlinear centre velocity response

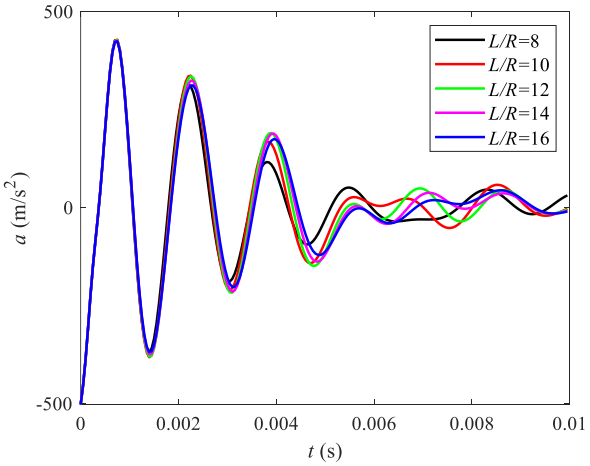

c) The nonlinear centre acceleration response

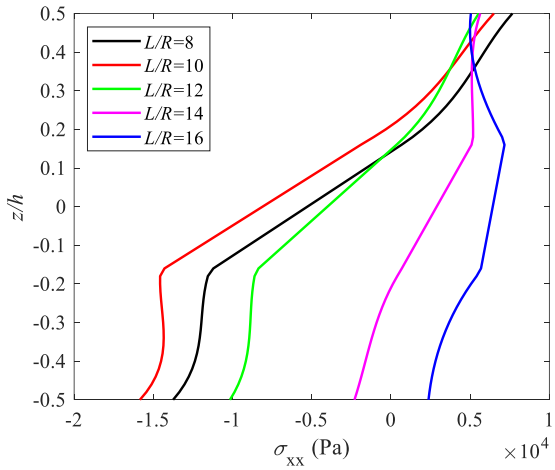

d) The normal stress $\sigma_{xx}(\frac{a}{2},\frac{b}{2},z)$ at the peak-point

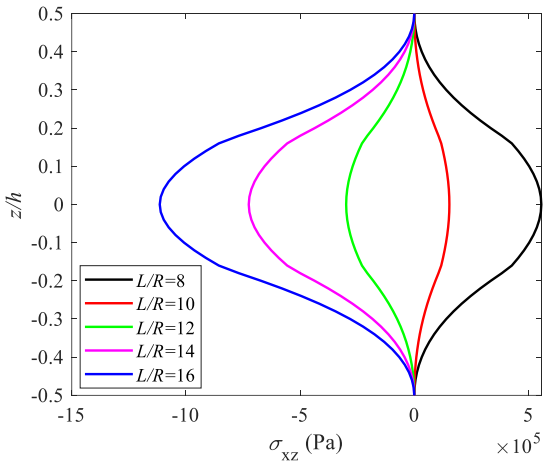

e) The shear stress $\sigma_{xz}(0,\frac{b}{2},z)$ at the peak-point

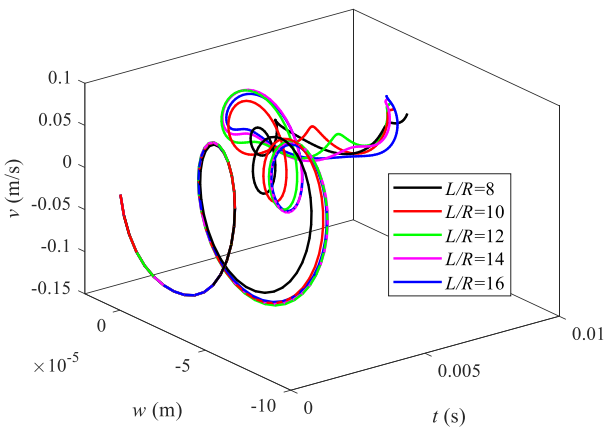

f) Phase orbit (3D-view)

Figure 10 The nonlinear response of CC FGhCS shells (1:1:1) under EL versus H/R ratio with $R = 2$ m, $L = 10R, h = R/10$, and $n = 2$.

4. CONCLUSION

This study presented an effective numerical framework for analyzing the nonlinear dynamic of FGhCS shells with elastic boundary conditions subjected to explosive loading. The governing equations were derived based on the MITC4 finite element formulation, and a MATLAB code was developed to efficiently capture the nonlinear dynamic response of FGhCS shells. The proposed approach effectively eliminates shear-locking effects, satisfies the shell boundary zero shear stress condition, and achieving high computational efficiency without compromising accuracy.

The parametric investigations revealed that both material properties and geometric configuration critically influence the nonlinear dynamic behavior of FGhCS shells, while elastic boundary stiffness plays an equally decisive role in governing their dynamic response. An increase in the power-law index n enhances the ceramic content, leading to higher stiffness and natural frequencies, whereas thicker metallic cores reduce overall rigidity and frequency. The thickness ratio $h_1{:}\,h_2{:}\,h_3$ and geometric slenderness L/R significantly affect nonlinear deformation and stability–larger L/R values diminish curvature-induced stiffness, resulting in greater deflection amplitudes. Furthermore, the study demonstrates that elastic supports fundamentally modify the deformation mechanism compared with idealized fixed or simply supported edges. The boundary stiffness directly governs load transfer and strain-energy distribution along the edges, allowing partial compliance that can either amplify or suppress deflection depending on the geometric configuration. These findings emphasize that realistic boundary modeling is indispensable for accurately capturing the true mechanical behavior of FGhCS shells operating in complex service environments.

Overall, the interplay among material properties, geometric parameters, and boundary flexibility defines the global stiffness–stability balance of FGhCS structures. Optimizing these parameters enables the design of lightweight, thermally robust, and vibration-controlled FGM sandwich shells suitable for aerospace and marine applications. The present MITC4-based formulation has been rigorously validated against benchmark solutions, confirming its reliability for moderately thick FGhCS shells.

Despite the advantages of the proposed formulation, several limitations should be noted. First, the present model employs flat four-noded MITC4 elements, which are most suitable for shallow shell geometries with relatively large curvature radii. For highly curved shells, the accuracy may be affected by the geometric approximation inherent in flat elements. Second, the formulation is developed within the framework of the FSDT; therefore, its applicability is mainly limited to moderately thick shells, while extremely thick structures may require higher-order theories. In addition, the normal stresses presented in the numerical results are evaluated approximately at selected sampling locations within the elements, and thus they mainly reflect the overall stress trends rather than highly localized stress concentrations. These aspects may be addressed in future work by considering higher-order shell theories and curved shell finite elements. Experimental validation under realistic loading conditions–such as thermal gradients, impact, and shock excitations–will further consolidate the applicability of the proposed approach to advanced structural systems.

Author's Contributions: Writing - Reviewing & Editing, Supervision, Project administration, Methodology, Nhan Thinh Hoang and Quoc-Hoa Pham; Investigation, Writing Original draft, Software, Methodology, Ngoc Anh Vu and Trung Thanh Tran; Investigation, Writing Original draft, Software, TD Pham and Truong Son Le.

Data availability: Research data is available in the body of the article.

Editor: Pablo Andrés Muñoz Rojas

References

Alibeigloo, A., & Alizadeh, M. (2015). Static and free vibration analyses of functionally graded sandwich plates using state space differential quadrature method. *European Journal of Mechanics-A/Solids*, *54*, 252-266.

Chen, H., Wang, A., Hao, Y., & Zhang, W. (2017). Free vibration of FGM sandwich doubly-curved shallow shell based on a new shear deformation theory with stretching effects. *Composite Structures*, *179*, 50-60.

Chung, H. (1981). Free vibration analysis of circular cylindrical shells. *Journal of Sound and Vibration*, *74*(3), 331-350.

Dang, X.-H., Nguyen, V.-L., Tran, M.-T., & Nguyen Thi, B.-P. (2022). Free vibration characteristics of rotating functionally graded porous circular cylindrical shells with different boundary conditions. *Iranian Journal of Science and Technology, Transactions of Mechanical Engineering*, *46*(1), 167-183.

Do, N.-T., Dang, H. T., Tran, T. T., Du, N. V., & Pham, Q. H. (2025). Dynamic response-based isogeometric analysis of graphene platelets-reinforced functionally graded triply periodic minimal surface plates supported by Pasternak foundation. *Alexandria Engineering Journal*, *110*, 245-260.

Do, N.-T., & Tran, T. T. (2024). Random vibration analysis of FGM plates subjected to moving load using a refined stochastic finite element method. *Defence Technology*, *34*.

Do, N.-T., & Tran, T. T. (2026). Stochastic dynamic analysis of FGSW plates resting on a Pasternak foundation under a moving mass considering parameter uncertainties. *Next Materials*, *11*, 101687.

Duc, N. D., Seung-Eock, K., & Chan, D. Q. (2018). Thermal buckling analysis of FGM sandwich truncated conical shells reinforced by FGM stiffeners resting on elastic foundations using FSDT. *Journal of Thermal Stresses*, *41*(3), 331-365.

Dvorkin, E. N., & Bathe, K. J. (1984). A continuum mechanics based four-node shell element for general non-linear analysis. *Engineering computations*, *1*(1), 77-88.

Gupta, N., Sheriff, N. M., & Velmurugan, R. (2008). Experimental and theoretical studies on buckling of thin spherical shells under axial loads. *International Journal of Mechanical Sciences*, *50*(3), 422-432.

Hosseini-Hashemi, S., Taher, H. R. D., Akhavan, H., & Omidi, M. (2010). Free vibration of functionally graded rectangular plates using first-order shear deformation plate theory. *Applied Mathematical Modelling*, *34*(5), 1276-1291.

Jin, G., Ye, T., Ma, X., Chen, Y., Su, Z., & Xie, X. (2013). A unified approach for the vibration analysis of moderately thick composite laminated cylindrical shells with arbitrary boundary conditions. *International Journal of Mechanical Sciences*, *75*, 357-376.

Karakoti, A., Pandey, S., & Kar, V. R. (2022). Nonlinear transient analysis of porous P-FGM and S-FGM sandwich plates and shell panels under blast loading and thermal environment. *Thin-Walled Structures*, *173*, 108985.

Kim, Y.-W. (2015). Free vibration analysis of FGM cylindrical shell partially resting on Pasternak elastic foundation with an oblique edge. *Composites Part B: Engineering*, *70*, 263-276.

Lam, N., Mendis, P., & Ngo, T. (2004). Response spectrum solutions for blast loading. *Electronic Journal of Structural Engineering*, *4*, 28-44.

Le, P. B., Do, D. N., & Tran, T. T. (2026). Quasi-3D dynamic analysis of functionally graded auxetic graphene-origami-reinforced plates on viscoelastic foundations under pulse loading. *Mechanics Research Communications*, 104643.

Le, P. B., & Tran, T.-T. (2024). Dynamic response of honeycomb-FGS shells subjected to the dynamic loading using non-polynomial higher-order IGA. *Defence Technology*, *37*, 149-161.

Leissa, A. W. (1973). Vibration of shells (NASA SP-288). *Washington, DC: US Government Printing Office*.

Li, J., Ren, H., & Ning, J. (2021). Deformation and failure of thin spherical shells under dynamic impact loading: Experiment and analytical model. *Thin-Walled Structures*, *161*, 107403.

Liu, N., & Jeffers, A. E. (2017). Isogeometric analysis of laminated composite and functionally graded sandwich plates based on a layerwise displacement theory. *Composite Structures*, *176*, 143-153.

Liu, P., Kaewunruen, S., Zhao, D., & Wang, S. (2018). Investigation of the dynamic buckling of spherical shell structures due to subsea collisions. *Applied Sciences*, *8*(7), 1148.

Loy, C., Lam, K., & Reddy, J. (1999). Vibration of functionally graded cylindrical shells. *International Journal of Mechanical Sciences*, *41*(3), 309-324.

Loy, C., Lam, K., & Shu, C. (1997). Analysis of cylindrical shells using generalized differential quadrature. *Shock and vibration*, *4*(3), 193-198.

Malekzadeh, P., & Heydarpour, Y. (2012). Free vibration analysis of rotating functionally graded cylindrical shells in thermal environment. *Composite Structures*, *94*(9), 2971-2981.

Mantari, J., & Soares, C. G. (2013). A novel higher-order shear deformation theory with stretching effect for functionally graded plates. *Composites Part B: Engineering*, *45*(1), 268-281.

Natarajan, S., & Manickam, G. (2012). Bending and vibration of functionally graded material sandwich plates using an accurate theory. *Finite Elements in Analysis and Design*, *57*, 32-42.

Neves, A., Ferreira, A. J., Carrera, E., Cinefra, M., Jorge, R. M. N., Mota Soares, C., & Araújo, A. L. (2017). Influence of zig-zag and warping effects on buckling of functionally graded sandwich plates according to sinusoidal shear deformation theories. *Mechanics of Advanced Materials and Structures*, *24*(5), 360-376.

Nguyen, T. H., Nguyen, T. T., Tran, T. T., & Pham, Q.-H. (2023). Research on the mechanical behaviour of functionally graded porous sandwich plates using a new C1 finite element procedure. *Results in Engineering*, *17*, 100817.

Nguyen, T. T., Le, T. S., Tran, T. T., & Pham, Q.-H. (2024). Buckling analysis of functionally graded porous variable thickness plates resting on Pasternak foundation using ES-MITC3. *Latin american journal of solids and structures*, *21*, e524.

Nguyen, T. T., Nguyen, T. H., Tran, T. T., & Pham, Q.-H. (2024). A new finite element procedure for the dynamic analysis of BDFGS plates located on pasternak foundation subjected to the moving oscillator load. *Iranian Journal of Science and Technology, Transactions of Mechanical Engineering*, *48*(3), 1263-1281.

Nguyen, V. C., Tran, T. T., Nguyen-Thoi, T., & Pham, Q.-H. (2022). A novel finite element formulation for static bending analysis of functionally graded porous sandwich plates. *Frontiers of Structural and Civil Engineering*, *16*(12), 1599-1620.

Pham, Q.-H., Tran, T. T., & Nguyen, P.-C. (2023). Dynamic response of functionally graded porous-core sandwich plates subjected to blast load using ES-MITC3 element. *Composite Structures*, *309*, 116722.

Pradhan, S., Loy, C., Lam, K., & Reddy, J. (2000). Vibration characteristics of functionally graded cylindrical shells under various boundary conditions. *Applied Acoustics*, *61*(1), 111-129.

Qin, Z., Pang, X., Safaei, B., & Chu, F. (2019). Free vibration analysis of rotating functionally graded CNT reinforced composite cylindrical shells with arbitrary boundary conditions. *Composite Structures*, *220*, 847-860.

Reddy, J. (2000). Analysis of functionally graded plates. *International Journal for numerical methods in engineering*, *47*(1-3), 663-684.

Reddy, J. N. (2003). *Mechanics of laminated composite plates and shells: theory and analysis*. CRC press.

Reddy, J. N. (2015). *An Introduction to Nonlinear Finite Element Analysis: with applications to heat transfer, fluid mechanics, and solid mechanics*. Oxford university press.

Shen, Z., Xia, J., & Cheng, P. (2019). Geometrically nonlinear dynamic analysis of FG-CNTRC plates subjected to blast loads using the weak form quadrature element method. *Composite Structures*, *209*, 775-788.

Shu, C., & Du, H. (1997). Free vibration analysis of laminated composite cylindrical shells by DQM. *Composites Part B: Engineering*, *28*(3), 267-274.

Talha, M., & Singh, B. (2010). Static response and free vibration analysis of FGM plates using higher order shear deformation theory. *Applied Mathematical Modelling*, *34*(12), 3991-4011.

Trai, V. K., Van Huong Binh, N., & Tran, T. T. (2025). The vibration behaviour-based meshfree moving Kriging method of functionally graded sandwich plates placed on Kerr foundation. *Nondestructive Testing and Evaluation*, *40*(12), 5997-6025.

Tran, M.-T., Nguyen, V.-L., Pham, S.-D., & Rungamornrat, J. (2020). Free vibration of stiffened functionally graded circular cylindrical shell resting on Winkler–Pasternak foundation with different boundary conditions under thermal environment. *Acta mechanica*, *231*(6), 2545-2564.

Tran, T. T. (2026). Dynamic Response of Honeycomb Core Sandwich Plates assuming Sinusoidal Top Face Sheet Subjected to Half-Car Moving Load Resting on Elastic Foundation. *Thin-Walled Structures*, 114486.

Tu, T. M., & Loi, N. V. (2016). Vibration analysis of rotating functionally graded cylindrical shells with orthogonal stiffeners. *Latin american journal of solids and structures*, *13*(15), 2952-2969.

Wang, Y., & Wu, D. (2017). Free vibration of functionally graded porous cylindrical shell using a sinusoidal shear deformation theory. *Aerospace Science and Technology*, *66*, 83-91.

Yaghoobi, H., & Fereidoon, A. (2014). Mechanical and thermal buckling analysis of functionally graded plates resting on elastic foundations: An assessment of a simple refined nth-order shear deformation theory. *Composites Part B: Engineering*, *62*, 54-64.

Yin, F., Zhi, X., Fan, F., Wei, W., & Zheng, D. (2023). Blast loads and variability on cylindrical shells under different charge orientations. *Scientific reports*, *13*(1), 6719.

Zarga, D. (2019). Thermomechanical bending study for functionally graded sandwich plates using a simple quasi-3D shear deformation theory. *Steel and Composite Structures, An International Journal*, *32*(3), 389-410.

Zenkour, A. M. (2013a). Bending analysis of functionally graded sandwich plates using a simple four-unknown shear and normal deformations theory. *Journal of Sandwich Structures & Materials*, *15*(6), 629-656.

Zenkour, A. M. (2013b). A simple four-unknown refined theory for bending analysis of functionally graded plates. *Applied Mathematical Modelling*, *37*(20-21), 9041-9051.